2018

Compositional and Topographical Characterization of Carbonaceous Chondritic Meteorites Moss and Murray Using micro-Raman Spectroscopy and SEM/EDS

Aaron Stokke
Minnesota State University, Mankato

Compositional and Topographical Characterization of Carbonaceous Chondritic Meteorites Moss and Murray using micro-Raman Spectroscopy and SEM/EDS

By

Aaron R. Stokke

A Thesis Submitted in Partial Fulfillment of the

Requirements for the Degree of

Master of Science

In

Physics

Minnesota State University, Mankato

Mankato, Minnesota

June 2018

06/22/2018

Compositional and Topographical Characterization of Carbonaceous Chondritic Meteorites Moss and Murray using micro-Raman Spectroscopy and SEM/EDS

Aaron R. Stokke

This thesis has been examined and approved by the following members of the student's committee.

_____
Dr. Analía Dall'Asén, Advisor

_____
Dr. Russell Palma, Committee Member

_____
Dr. Chad Wittkop, Committee Member

Compositional and Topographical Characterization of Carbonaceous Chondritic Meteorites Moss and Murray using micro-Raman Spectroscopy and SEM/EDS

Aaron R. Stokke
Master of Science in Physics
Minnesota State University, Mankato
2018

Abstract

Carbonaceous chondritic meteorites are considered some of the most primitive surviving materials from the formation of our solar system. Thus, these objects can provide information about planet formation through their physical properties (such as structure, composition, and morphology) which can be characterized using microscopy and spectroscopy techniques. In this work, the analytical methods of Raman spectroscopy, scanning electron microscopy (SEM), energy-dispersive X-ray spectroscopy (EDS), and optical microscopy are applied to determine the mineralogical, topographical, and elemental compositions of two carbonaceous chondritic fragments: Moss and Murray. Both samples were comprised of chondrules and matrix while Moss contained chondrule rims and Murray included olivine crystals. Minerals found in Moss were graphitic carbon, forsterite (Mg-rich olivine), and enstatite (Mg-rich pyroxene) inside of the inclusions and graphitic carbon, forsterite, enstatite, hematite, and magnetite in the matrix. Murray's inclusions contained forsterite and enstatite, its matrix was comprised of primarily graphitic carbon, and both the inclusions and matrix included unidentified minerals. All of the identified, aforementioned minerals have been found in other carbonaceous meteorites. Both samples were composed of the same main elements (O, Fe, Mg, Si – over 10 wt. %) and both also included the same secondary elements (C, S, Ni, Ca, Al, Na, Cr – less than 10 wt. %). The element percentages by weight were in good agreement with the compositions observed in their respective meteorite classifications (CO for Moss and CM for Murray). Analyzing the Raman spectra of graphitic carbon in both samples showed that Moss had undergone more thermal metamorphism on its parent body than Murray which agrees with current petrologic schemes (3.6 for Moss and 2 for Murray). The results from this study contribute detailed information about the compositions of these chondritic meteorites and add to the research that has already been conducted on extra-terrestrial materials.

Table of Contents

1. Introduction

1.1 The Big Picture

The formation of the planets in our solar system is not fully understood and their origin is one of the most fundamental questions being researched (Hutchison 2004; Scott 2007; Sears 2005). Chondritic meteorites, or chondrites, are some of the most primitive materials in our solar system (Dall'Asén et al. 2017a; Scott 2007) with formation estimates up to ~4500 Ma (McSween et al. 2006 and references therein). In particular, carbonaceous chondrites are some of the most pristine chondrites and are easily accessible on Earth, so no space exploration is needed (Dodd 1981). Understanding these chondrites can unveil information about presolar materials, processes in the solar nebula, and planet formation (Bonal et al. 2016; Scott 2007).

Chondritic meteorites are composed of ancient inclusions (e.g. chondrules, calcium-aluminum-rich inclusions, crystal grains, etc.) and the matrix that surrounds and holds these inclusions together (Hutchison 2004). Studying the properties (e.g. chemical and elemental compositions, structure, and topography) of these inclusions and surrounding matrix can help in understanding the thermal, barometric, and temporal conditions in which the chondrites formed and the secondary processes they encountered on their parent bodies (Rubin 2010; Scott 2007; Wood 2005).

Several analytical techniques have been used to study these different properties in various samples. In particular, Raman spectroscopy has been used to study the mineralogical compositions, as well as scanning electron microscopy (SEM) and energy-dispersive X-ray spectroscopy (EDS) to study the morphological structures and elemental

compositions, respectively, of carbonaceous chondrite fragments (Bonal et al. 2006; Dall'Asén et al. 2017a; Metzler 2004; Quirico et al. 2005; Zolensky et al. 1997). In this study, these techniques are used to examine the properties of two carbonaceous chondritic meteorites, Moss and Murray. To the best of this research group's knowledge, a relatively small number of works have studied the compositions of these samples using the aforementioned techniques (Bernatowicz et al. 1987; Bouvier et al. 2013; Palmer and Lauretta 2011; Quirico et al. 2009; Yesiltas et al. 2016). The results obtained are utilized to identify their compositions in detail and some of these findings have already been presented (Dall'Asén et al. 2018). Possible explanations about the conditions in which these relics were formed and how they were affected by secondary processes are also briefly discussed.

1.2 Meteorite Samples

1.2.1 Meteorites

The solar system contains natural, interplanetary objects of varying sizes and origins. If the approximate diameter of the entity is between 10 μm and 1 m it is termed a meteoroid (Rubin and Grossman 2010). Occasionally. meteoroids enter the Earth's (or any celestial body's) atmosphere and are heated, producing streaks of light called meteors (Hutchison 2004). If the meteoroid survives this intense heating period and reaches the surface, the resulting solid material is defined as a meteorite (Campbell-Brown and Brown 2016).

The parent bodies of meteorites consist of asteroids, planets, comets, natural satellites, and objects from outside the solar system. Of the meteorites found on Earth, it is estimated that 99.8% come from asteroids with the remaining 0.2% having lunar or Martian origins (nasa.gov). There is no definitive consensus if meteorites found on Earth originated from comets (Hutchison 2004).

The discovery of meteorites can be classified as either falls or finds. Falls are directly observed as they travel through the atmosphere and can be recovered very quickly after they land. Finds are not observed and are usually found long after they have landed on the surface. In either case, meteorites can often be distinguished from terrestrial rocks by a fusion crust – a one to three millimeter layer of material on the meteorite surface that melted and re-solidified during its travel through the atmosphere (Hutchison 2004).

1.2.2 Classification Scheme

Meteoritic taxonomy is very complex, so the following is a simplified scheme highlighting the classifications of the samples used in this work. Figure 1.1 displays a classification tree based on the text by Hutchison (2004) and the paper by Weisberg et al. (2006).

Meteorites are first categorized into three types: stony, iron, and stony-iron. Stony meteorites are mainly composed of silicates, iron meteorites are primarily iron-nickel metal, and stony-iron have approximately even amounts of both (Dodd 1981). The stony meteorites are further categorized into two subtypes: chondrites and achondrites. Chondrites contain chondrules (Section 1.2.3), originated on meteorites that were subjected

to little or no melting, and are considered some of the most primitive materials in the solar system. Achondrites are chemically dissimilar to chondrites, do not have chondrules, and experienced more alteration while on their parent bodies (Hutchison 2004; Scott 2007).

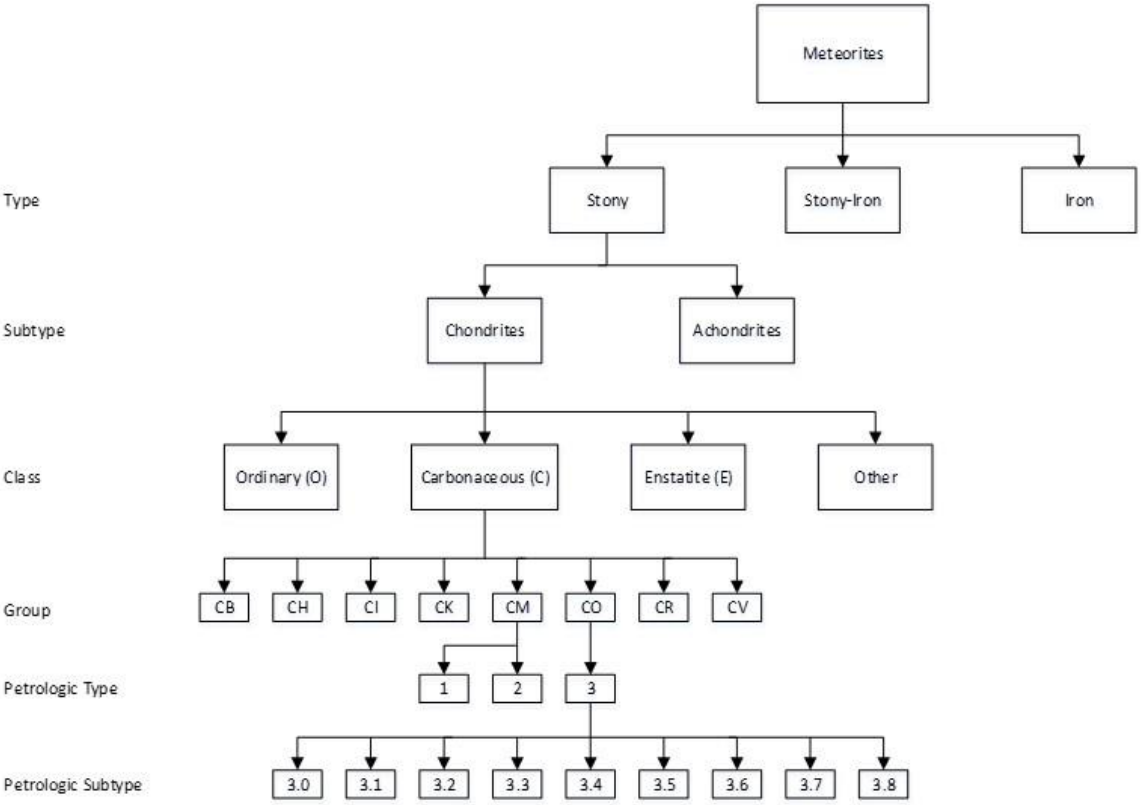

Figure 1.1: Meteorite classification tree (adaptation/combination of Hutchison 2004 and Weisberg et al. 2006).

The chondrites subgroup is divided into different classes with the main ones known as ordinary, carbonaceous, and enstatite. The ordinary chondrites get their name because most of the falls and finds of stony meteorites are in this class. The members of this class have very similar ratios of Mg to Si and Ca/Al/Ti to Si. When first discovered, the carbonaceous chondrites were thought to be the only class to contain carbon. Despite what their name seems to imply, these meteorites only contain <1 to ~6 wt. % carbon (Scott 2007). The carbonaceous class is considered the most primitive of the classes as

their ratio of nonvolatile elements (Fe, Si, Mg, Al, Ca, etc.) is very similar to that of the sun (Dodd 1981). The enstatite chondrites are relatively rare and nearly all of their iron is in the form of metal or iron sulfide. Most of the pyroxene in this group is the Mg-rich enstatite, from which the class get its name (Norton and Chitwood 2008). A very small number of chondrites do not meet any of the listed criteria and have too few members to make up any new classes and thus are classified here as "other".

Inside of the carbonaceous chondrite class, eight different groups emerge: CB, CH, CI, CK, CM, CO, CR, and CV. The preceding "C" indicates the carbonaceous nature of the meteorite. The second letter specifies the location where the most prominent meteorite with similar composition originated (Weisberg et al. 2006). For example, CM chondrites are connected in composition to the Mighei (Ukraine) meteorite and the CO chondrites are related compositionally to the Ornans (France) meteorite. The only exception to this two-letter system is the CH group, where the "H" stands for "high metal" (Hutchison 2004).

The carbonaceous chondrite class also contains petrologic (some authors use the term "petrographic") types based on the secondary processes (aqueous alteration or thermal metamorphism) subjected to the parent body (Bonal et al. 2006). These types are assigned a number from 1 to 7 (Fig. 1.2) which is appended to the two-letter system used for group

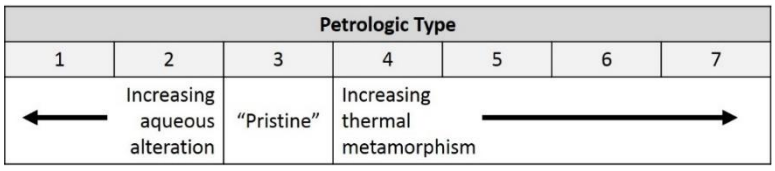

Figure 1.2: Petrologic sequence for chondrites (adapted from Norton and Chitwood 2008 and McSween 2010).

identification. Meteorites of petrologic type 3 are considered the most pristine samples as they are the least altered relative to the other types. From types 2 to 1 the amount of aqueous alteration increases, and thermal metamorphism increases from 4 on up (Norton and Chitwood 2008; Weisberg et al. 2006).

Petrologic type 3 can be further split into subtypes based on another scale involving thermal metamorphism. Petrologic subtypes are allocated decimal values (from 3.0 to 3.8) with thermal alteration increasing from lower to higher values (Chizmadia et al. 2002). Research indicates that the type 3 chondrites were heated to peak temperatures between ~350° and 600°C (Huss et al. 2006; Hutchison 2004; McSween, Jr. and Huss 2010; Norton and Chitwood 2008; Scott 2007).

1.2.3 Chondritic Components

As stated in the previous section, chondrites are a specific subtype in the meteoritic classification scheme. Other than the CI group, all of the carbonaceous chondrites contain chondrules (Hutchison 2004). These are ovoid or spherical grains on the order of a few millimeters or smaller in size that are typically composed of crystallized silicates (Dodd 1981). Another type of chondritic inclusion is whole or fragmented crystals of olivine and/or pyroxene (Hutchison 2004). Chondrules and inclusions are surrounded by matrix, which is finely grained filler material (of approximately micron sized particles) that holds the different chondrules and inclusions in place (Scott 2007).

1.3 Raman Spectroscopy

1.3.1 Theory

Elastic and inelastic scattering events occur when a photon interacts with a material. In an elastic scattering event the kinetic energy of the photon is conserved – the photon's kinetic energy is the same both before and after the interaction. Conversely, the kinetic energy of the photon is not conserved in an inelastic scattering event – the photon gives up or takes some energy from the material, so the initial and final photon energies are different (Serway and Jewett 2009). In vibrational spectroscopy, elastic and inelastic events are termed Rayleigh and Raman scattering, respectively.

Raman scattering involves the vibrational energy of bonds between the atoms that make up a molecule. As a result of quantum mechanics, these vibrational energy levels can only have discrete values and are therefore unique to each molecule. These characteristic frequencies (corresponding to their respective energies) are sometimes referred to as molecular "fingerprints". The frequencies of molecular vibrations depend on the atomic masses, molecular geometry, and the strength of the bonds connecting atoms (Larkin 2011).

The electron cloud surrounding a molecule is the probabilistic representation of the electrons associated with the atoms that make up the molecule. If there is a tendency for the positive and negative charges to build up on one side or the other (due to the electron distribution and the molecular geometry), the molecule is said to be polarized (Serway and Jewett 2009). Raman scattering occurs due to a change in the polarization of a molecule. When a molecule is placed in an external electric field, deformation of the surrounding

electron cloud may occur. Greater alteration of the cloud leads to a greater intensity of the Raman signal. If the presence of an external field does not induce a change in the electron cloud, then the molecule is said to be Raman inactive (Larkin 2011).

In order to achieve the aforementioned scattering events, an excitation source irradiates a sample with photons of some initial frequency ν_i. This excites a molecule in the sample to some virtual energy state, below the first excited electronic state. This unobservable virtual state decays extremely quickly and therefore does not violate the energy-time uncertainty principle. When the excited molecule returns to a lower energy

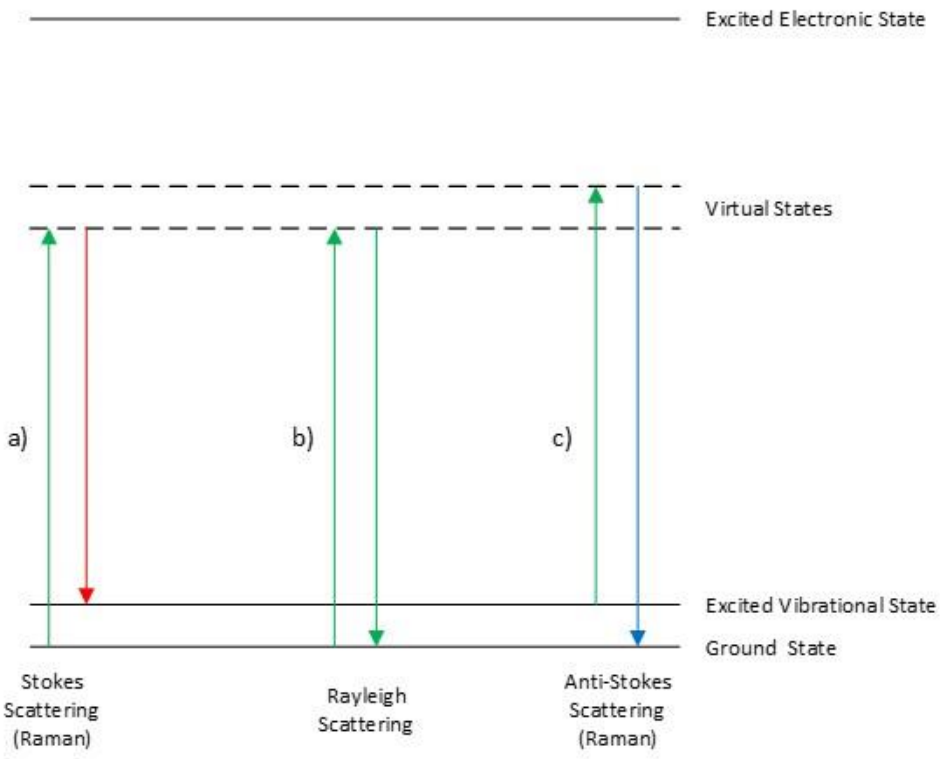

Figure 1.3: Energy level diagram (not to scale) illustrating vibrational energy transitions of molecules in Raman spectroscopy. The incident photon energy is represented by the arrow pointing "up". The scattered photon energy is represented by the arrow pointing down and has a) a lower frequency ($\nu_i - \nu_s$), b) the same frequency (ν_i), and c) a higher frequency ($\nu_i + \nu_s$) compared to the incident photon.

state it produces a photon with the same frequency ν_i (Rayleigh scattering), lower frequency $\nu_i - \nu_s$ (Raman Stokes scattering), or higher frequency $\nu_i + \nu_s$ (Raman anti-Stokes scattering) as compared to the incident radiation (Fig. 1.3). At room temperature, there is a higher probability of molecules being in the ground state than an excited state so Stokes lines have a greater intensity than anti-Stokes lines (Ferraro et al. 2002; Raman 1929).

A quantity related to the frequency of the scattered photons is called the wavenumber $\tilde{\nu}$, and is defined by the equation:

$$\tilde{\nu} = \frac{\nu}{c} = \frac{1}{\lambda} \tag{1.1}$$

where ν is the photon frequency, λ is the photon wavelength, and c is the speed of light. The essential quantity for molecular identification is the Raman shift wavenumber $\Delta\tilde{\nu}$, which is given by the equation:

$$\Delta\tilde{\nu} = \tilde{\nu}_i - \tilde{\nu}_s = \frac{1}{\lambda_i} - \frac{1}{\lambda_s} \tag{1.2}$$

where $\tilde{\nu}_i$, λ_i and $\tilde{\nu}_s$, λ_s represent the properties of the incident and Raman scattered photons, respectively. Assuming the wavelengths are known in nanometers, then the appropriate conversion of $\frac{10^7 \text{nm}}{1 \text{ cm}}$ can be used to get cm^{-1}, the common Raman shift wavenumber unit. A great advantage of using the Raman shift wavenumber is that it is independent of excitation source and therefore peaks will always occur at the same position regardless of the excitation wavelength (Ferraro et al. 2002). Figure 1.4 illustrates a Raman spectrum for industrial diamond with a characteristic peak position at ~1335 cm^{-1}.

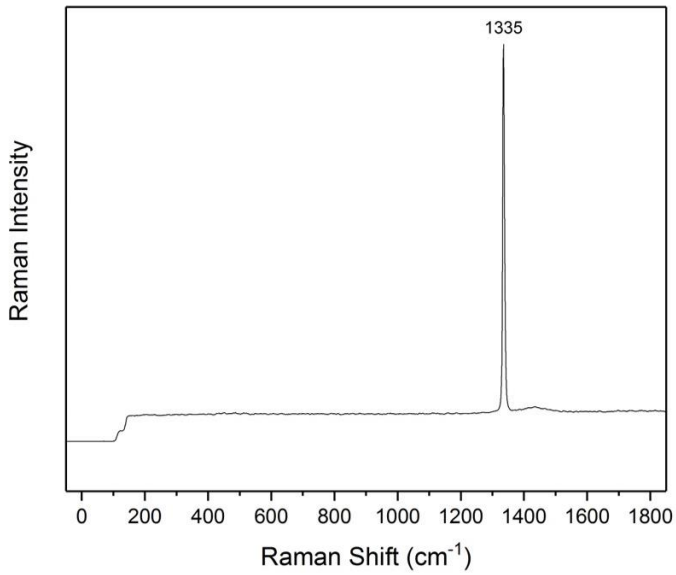

Figure 1.4: Raman spectrum for industrial diamond with characteristic peak position at ~1335 cm^{-1}.

1.3.2 Typical Instrument Components

Raman spectroscopy systems commonly include the following components. The excitation source is usually a continuous-wave laser in the near-IR, visible, or near-UV ranges. The beam is directed with the corresponding optics (e.g. lenses, mirrors, filters, etc.) to irradiate the sample with the appropriate power. After interacting with the sample, the scattered light is collected with optics and sent to a prism or diffraction grating to break the signal down into its corresponding wavelengths. This new signal is sent to a detector (e.g. a photomultiplier tube or charge-couple device) and the output is displayed on a computer monitor (Ferraro et al. 2002).

1.3.3 Applications

A convenient feature of Raman spectroscopy is its ability to measure spectra from many different types of materials including gases, liquids, solutions, crystals, and

amorphous solids. Another advantage is that it is a non-destructive technique and does not require special preparation, so the sample can be reanalyzed using different methods after Raman spectroscopy has been performed. Numerous fields such as physics, materials science, chemistry, biochemistry, medicine, and pharmacy have found uses for the technique. Some examples of application in both research and industry include: determining polymorphs and phase transitions of solids, detecting hazardous materials in ground water, diagnosing malignant tissues in the human body, and identifying illicit drugs (Ferraro et al. 2002).

1.4 Scanning Electron Microscopy (SEM)

1.4.1 Theory

Analogous to the photon cases mentioned earlier (Section 1.3.1), electrons experience scattering events during interactions with a material. When an electron enters a sample, its trajectory can be altered by the net positive charge associated with an atom resulting in elastic scattering. A second option is that an incoming electron expels an electron from the surrounding cloud which gives rise to inelastic scattering (Goldstein et al. 2018).

If one (or multiple) interactions change the electron's path by 180°, the electron exits the sample and is called a backscattered electron (BSE). Since backscattering is an elastic phenomenon, the energy of the electron is approximately the same before and after the event (usually on the order of 10 keV). This relatively high energy allows the BSEs to have a larger escape depth than the inelastically scattered electrons (Fig. 1.5). The

subsequent signal allows for images to have compositional contrast, as elements with higher atomic numbers produce more BSEs (Goldstein et al. 2018; Hafner 2015a).

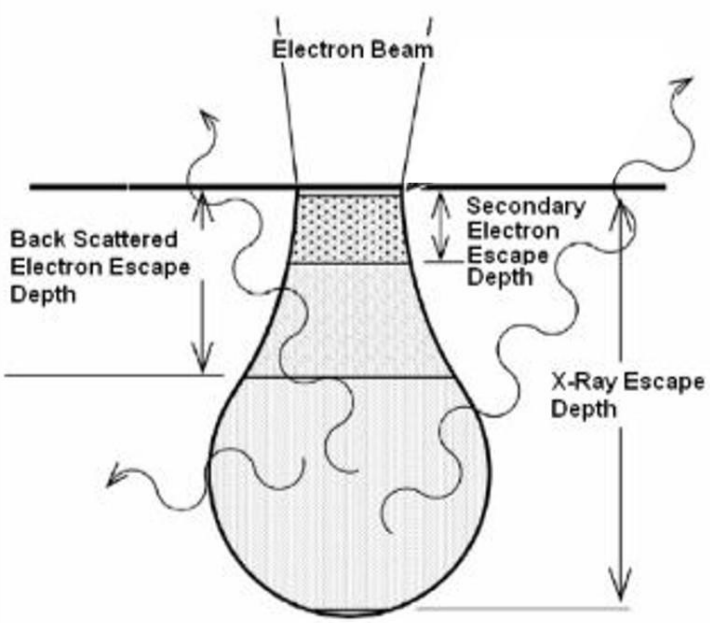

Figure 1.5: Schematic demonstrating the relative escape depths (not to scale) of electrons and characteristic X-rays in a sample (original image from Hafner 2015).

If the interaction causes an electron to be knocked out of the surrounding cloud, the expelled electron is called a secondary electron (SE). The incident electron loses a very small percentage of its initial energy in the interaction and the inelastically scattered SE has relatively low kinetic energy (on the order of a few eV). This lower energy results in a shallower escape depth and gives SE images topographical contrast, so the structure of the sample can be analyzed (Goldstein et al. 2018; Hafner 2015a). Figure 1.6 demonstrates as SE image of the same industrial diamonds used for the Raman spectroscopy example (Fig. 1.4).

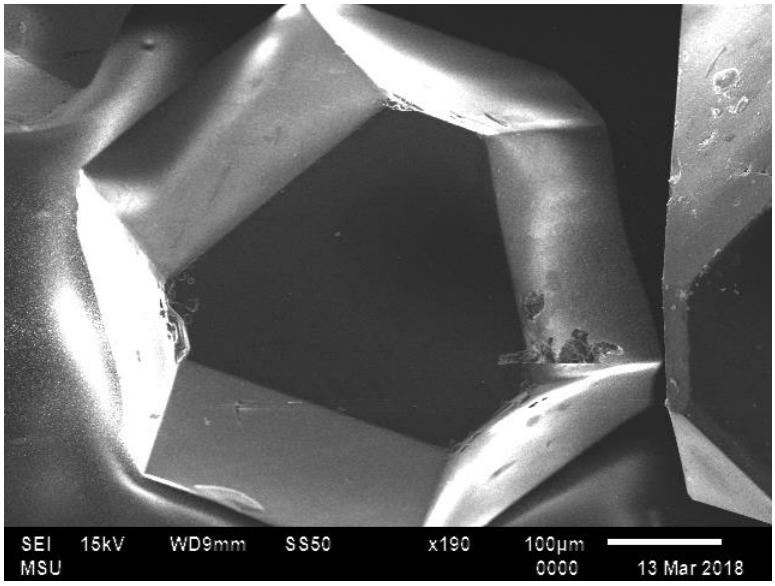

Figure 1.6: Secondary electron image of industrial diamonds mounted on a silicon wafer.

1.4.2 Typical Instrument Components

Common components of SEM/EDS systems include the following. The excitation source is an electron gun which accelerates the beam of electrons toward the sample. The beam diameter and focus are controlled by an arrangement of electromagnetic lenses to irradiate the sample. Once the electrons have interacted with the sample, the electron and X-ray signals are collected by their respective detectors. These signals are then sent to a computer monitor for viewing (Hafner 2015a).

1.4.3 Applications

Like Raman spectroscopy, SEM is a non-destructive technique. However, it does require special preparation (a conductive coating) in samples that have low electrical conductivity. This technique has various applications in both research and industry including the following (non-exhaustive): semiconductor failure analysis, memory device

inspection, cell and tissue investigation, and structure examination for many types of materials (Echlin et al. 1986; Shimizu and Mitani 2010).

1.5 Energy-Dispersive X-ray Spectroscopy (EDS)

1.5.1 Theory

In Section 1.4.1, two types of interactions between an electron beam and a material were described. If an electron beam ejects a SE from an inner shell, the atom is left in an excited state (since at room temperature, a majority of atoms in most materials are in the electronic ground state). Sometimes an electron drops down from a higher shell to fill the hole left by the SE. This produces an X-ray with energy given by the equation:

$$E_X = E_{in} - E_{out} \tag{1.3}$$

where the subscripts "in" and "out" corresponds to the binding energies of the inner and outer shell electrons, respectively. Since these energy levels are quantized, each element has its own unique values of E_X and the corresponding X-rays are called characteristic X-rays (Goldstein et al. 2018; Hafner 2015b). Figure 1.7 displays an elementary schematic of the production of characteristic X-rays.

1.5.2 Applications

It is common to find energy-dispersive spectrometers in conjunction with SEMs and the main use of EDS is to determine the elemental composition of a sample. The characteristic X-rays produced in a sample can be observed using a detector. Using

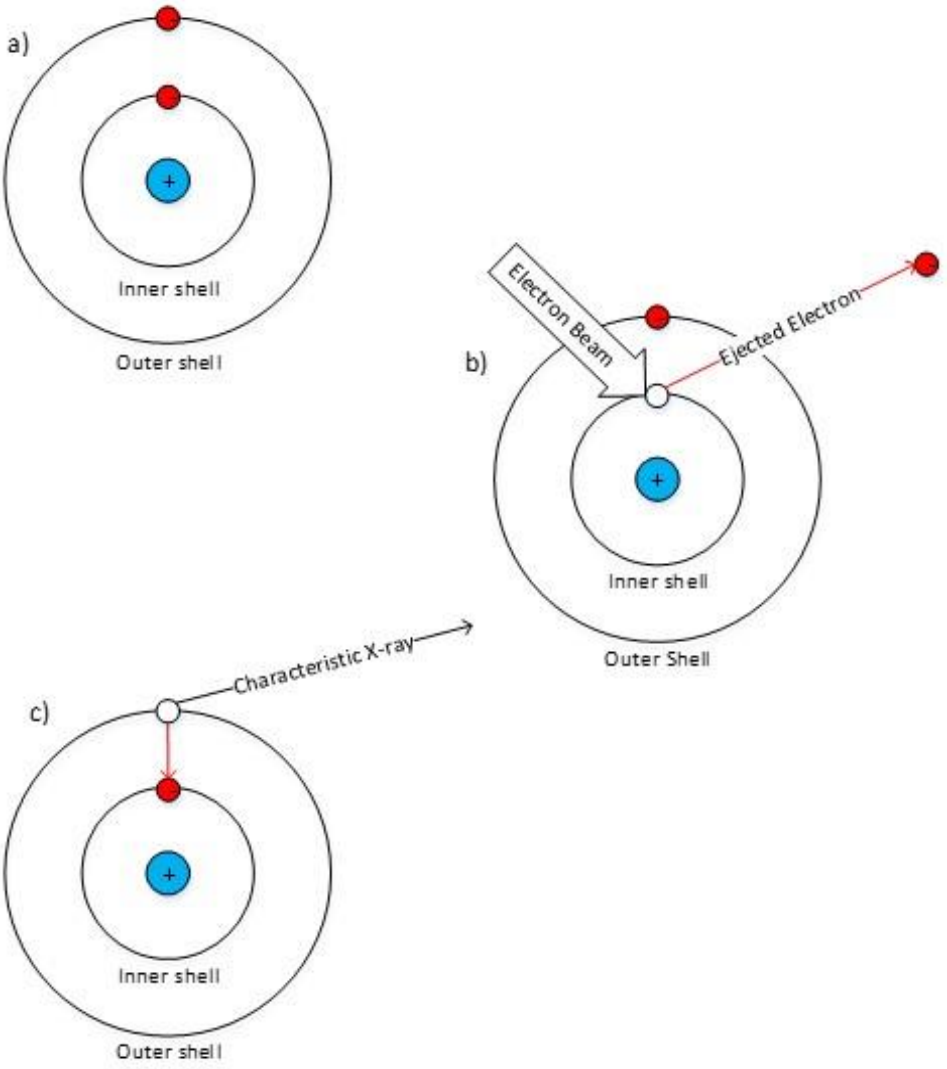

Figure 1.7: Cartoon illustrating the basics of characteristic X-ray production. a) The atom starts in the ground state; b) an electron beam ejects an inner shell electron; c) an X-ray is produced by an electron transition between the shells.

computer software X-ray spectra can be obtained, the origins of the X-rays can be mapped, and the percentage by weight of each element can be determined (Hafner 2015b). This research will use the convention of Goldstein et al. (2018) for major (>10 wt. %), minor (1-10 wt. %), and trace (<1 wt. %) elements. The X-ray spectrum (Fig. 1.8) and elemental

maps (Fig. 1.9) from the industrial diamond sample used previously for examples of Raman spectroscopy and SEM (Sections 1.3.1 and 1.4.1) can be seen below.

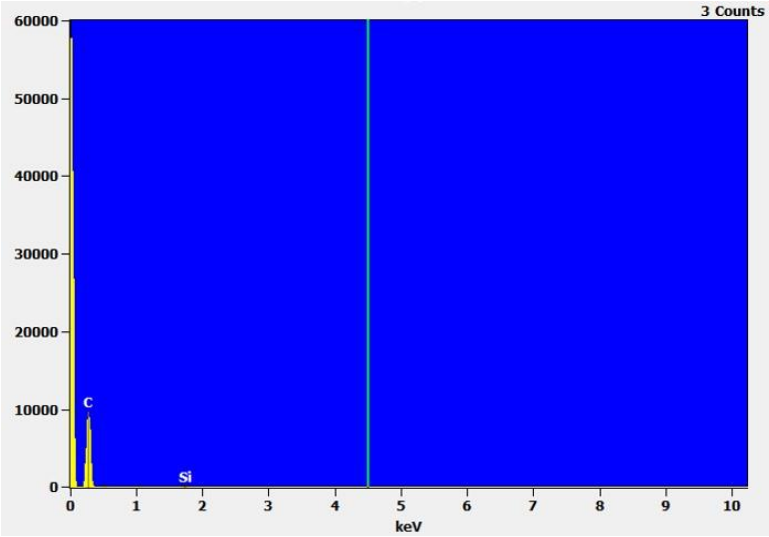

Figure 1.8: EDS spectrum for industrial diamond. The x-axis represents the energy of the X-ray (in keV) and y-axis represents the intensity of the signal (in counts) for a given energy. The vertical line at ~4.5 keV is the selection cursor from the data analysis software.

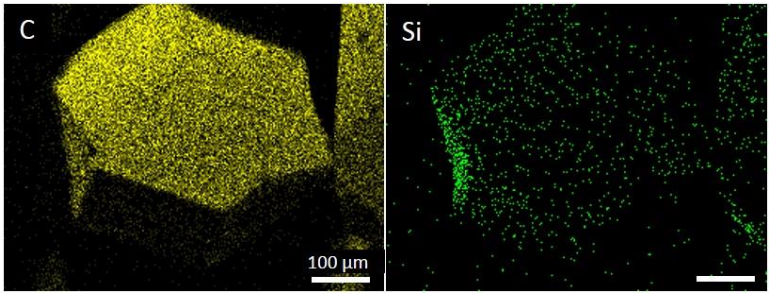

Figure 1.9: EDS element maps for industrial diamond (carbon-yellow, silicon-green). Quantitative analysis finds the sample is almost exclusively composed of carbon (99.26 wt. %). The small amount of silicon comes from the wafer on which the diamond is mounted.

2. Experimental Methods

Descriptions of the samples and the analytical methods used for this research are elaborated upon in the following sections. The main instruments used included: a Raman spectroscopy system and software and an SEM/EDS system and software. Also, an optical microscope (Nikon Eclipse ME600L) and software (PixeLINK μScope) were used for optical inspection of the samples (not described here). Methods used for data acquisition and analysis are also described.

2.1 Samples

Two meteoritic samples, Moss and Murray, were examined in this research. Both meteorites are members of the carbonaceous chondrite class but occupy different groups within that class. No sample preparation was needed since it was not required for Raman spectroscopy and the samples were conductive enough to not need special coating for the SEM/EDS.

2.1.1 Moss

The first sample analyzed came from the Moss meteorite (Fig. 2.1). On July 14, 2006 an observed meteorite fall was witnessed both visually and audibly by people near the Norwegian towns of Moss and Rygge. During the following month, searchers of the area unveiled five separate finds from this fall. The discoveries consisted of complete stones, half stones, fragments, and shattered pieces culminating in an approximate mass of 3.76 kg (Connolly et al. 2007). Since its fall, research of Moss has led to its classification

as a CO3.6 carbonaceous chondrite according to the Chizmadia et al. (2002) scheme (Section 1.2.2).

The 1.283-g partial slice from Moss was acquired from the online vendor, The Meteorite Market. The sample was cut on a diamond slab saw with 99% isopropyl alcohol used as coolant and was not polished in any way (Twelker 2018). It contained a very flat edge that was advantageous for taking data.

Figure 2.1: Moss CO3.6 meteorite sample used for this research.

2.1.2 Murray

The second sample analyzed came from the Murray meteorite (Fig. 2.2). On September 20, 1950 a meteorite fall was seen and heard by people in the states of Illinois and Kentucky. Many pieces from this fall were recovered to the east of Murray, Kentucky by local residents and a search team from Vanderbilt University through October of that same year (Horan 1953). Analysis of Murray has let to its classification as a CM2 carbonaceous chondrite (McSween 1979).

The 3.366-g fragmented piece from Murray was acquired from a colleague in the Department of Physics and Astronomy at Minnesota State University, Mankato. While

there is no explicit sign of polishing, it does contain a smooth surface from which data was taken. This flat surface allowed for quality measurements to be made from both the Raman system and the SEM/EDS.

Figure 2.2: Murray CM2 meteorite sample used for this research.

2.1.3 Selected Inclusions

Inclusions in the samples were chosen based on their optical and electron imaging potential. Many inclusions in both Moss and Murray were initially chosen, arbitrarily numbered starting at one, and then viewed with both the Raman probe video camera (Section 2.2.1) and the SEM. After inspecting the images, the most distinct inclusions (five from Moss and six from Murray) were selected for further analysis (Fig. 2.3). Once these inclusions were identified, six spots from each inclusion were designated for taking data – three from inside the inclusion and three from the surrounding matrix. Spots were selected to cover as many different qualitative features (e.g. color, structure, etc.) as possible.

Specific locations of the spots from each chondrule can be found from the figures in Sections 3.2.2 and 3.3.2.

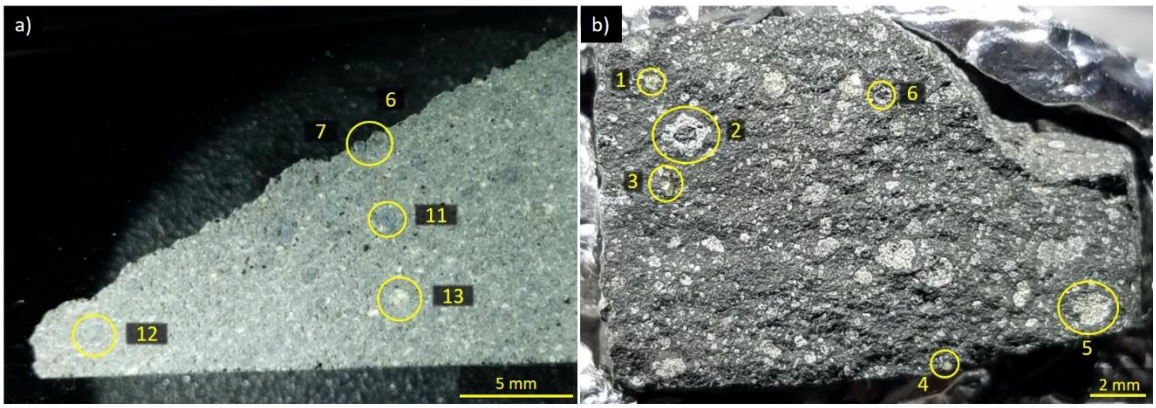

Figure 2.3: Samples with inclusions used for taking data marked with yellow circles. a) Moss CO3.6 b) Murray CM2.

2.2 Raman Spectroscopy

2.2.1 Experimental Setup and Procedure

The Raman spectroscopy system (Fig. 2.4) used for this research was custom built by Dr. Analía Dall'Asén (Department of Physics and Astronomy) and included the following main components: a solid-state laser (Coherent Sapphire SF 532 nm), a Raman probe equipped with a video camera, filters, mirrors, lenses, and microscope objective (Renishaw RP20V), a spectrograph (Andor SR-303i-A) with a CCD detector (Andor iDus DU401A-BVF), and a data acquisition computer workstation with spectrometer software (Andor Solis S). Auxiliary components of the system included optics, filters, stages, and power meters from either Semrock or Thorlabs.

Measurements were taken at room temperature and with a laser power at the sample of approximately 5 mW. After being redirected by the appropriate optics, the laser light

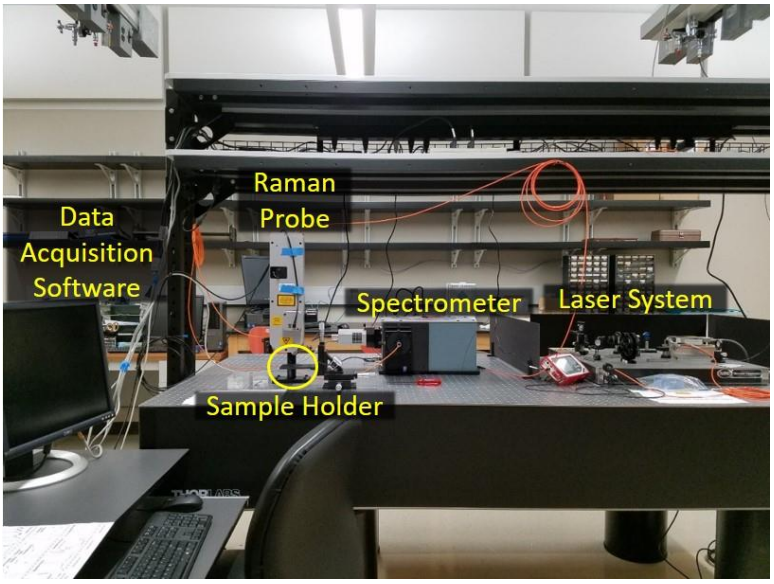

Figure 2.4: Laboratory setup for taking Raman spectroscopy data.

was transmitted through the Raman probe which consisted of a 10X objective lens with a numerical aperture of 0.25. The Raman probe camera was used to find the regions of interest and to make sure the laser spot was positioned at the appropriate locations. The beam was focused onto the sample and the scattered signal was collected by the same 10X lens (backscattering configuration). The Rayleigh scattering was filtered out and the Raman signal was directed to the spectrograph and charge-coupled device (CCD). After sorting this signal into its respective frequencies, the data was sent to the computer workstation to be compiled with the help of software (Fig. 2.5). Both high- (1200 lines/mm) and low-resolution (600 lines/mm) spectra were taken. The accumulation time was set for one second and five to one hundred accumulations were taken depending on the resolution and signal-to-noise ratio.

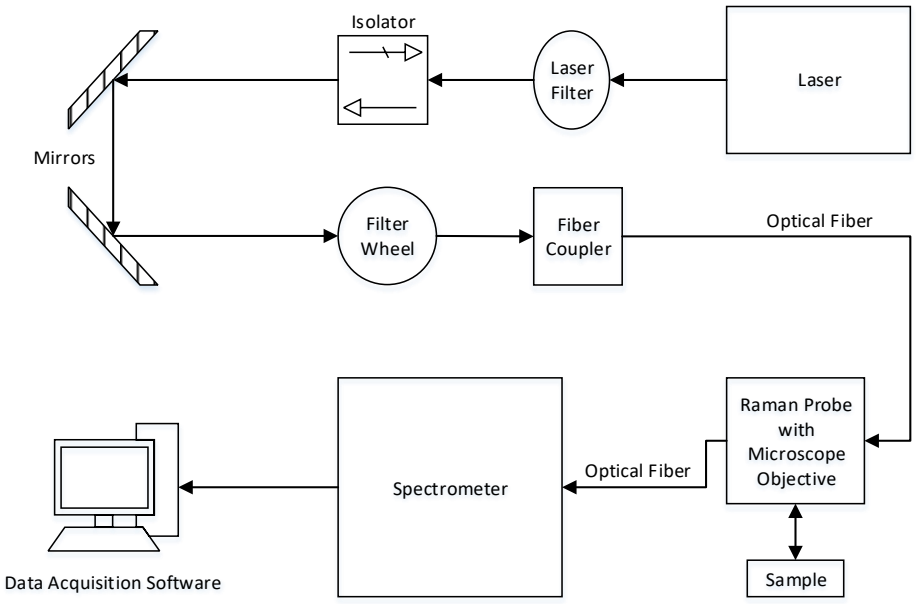

Figure 2.5: Schematic diagram of the Raman spectroscopy system.

If the power density of the laser at the sample surface was too high, then the heat produced could alter the sample. Dall'Asén et al. (2017a) and references therein give a relatively safe threshold for the power density value up to approximately 1300 W/mm^2. To find the minimum theoretical beam width w, the following equation can be used:

$$w = \frac{1.22\lambda}{\mathrm{NA}} \tag{3.1}$$

where λ is the excitation wavelength and NA is the numerical aperture of the objective lens. Using the values given in the previous paragraph, the minimum beam width w of this system is ~2.60*10^{-3} mm. The following trivial equation can be used to find the power density σ (power per unit area) of the laser spot on the sample:

$$\sigma = \frac{P}{A} = \frac{P}{\pi r^2} = \frac{4P}{\pi w^2} \tag{3.2}$$

where P is the laser power, A is the cross-sectional area of the beam at the sample, and r is the radius of the beam at the sample. Plugging in the values from before gives a power density σ of ~940 W/mm^2. Imperfections in the system would cause the beam diameter to be larger than the theoretical value, with estimates from 3 to 5 μm. This would cause the power density to drop, with values ranging from ~700 to ~250 W/mm^2, respectively. In any case, all of these values fall below the upper threshold given before.

2.2.2 Data Acquisition and Analysis

Once at the computer, the Solis S software was used to obtain spectra of the Raman shift (Stokes) wavenumbers. These spectra were then analyzed using the commercial software package, OriginPro 2017. The built-in "Gauss" fit was used which is an area version of the Gaussian function and is described by the following equation:

$$y = y_0 + \frac{A}{w\sqrt{\frac{\pi}{2}}} e^{-2\frac{(x-x_c)^2}{w^2}} \tag{3.3}$$

where y_0 is the offset, w is the peak width, x_c is the center position of the peak, and A is the area under the curve. The width is related to the more familiar quantities of standard deviation (σ) and full width at half maximum (FWHM) by:

$$w = 2\sigma = \frac{FWHM}{\sqrt{2\ln(2)}} \tag{3.4}$$

Figure 2.6 displays a Gaussian distribution from the OriginPro 2017 software package consisting all of the parameters given in Equations 3.3 and 3.4.

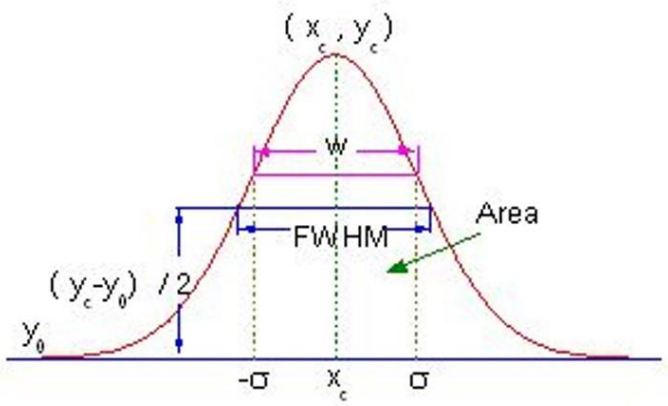

Figure 2.6: Plot of a typical Gaussian distribution.

2.2.3 Mineral Identification

After the Raman shift wavenumbers were determined for the spectra, the peak positions were compared to literature and online databases to determine what mineral was present. The primary database used was the RRUFF Project (rruff.info) maintained by the Department of Geosciences at the University of Arizona.

2.3 SEM/EDS

2.3.1 Experimental Setup and Procedure

The SEM/EDS system (Fig. 2.7) used for this research was housed in the Department of Biological Sciences and consisted of the following self-contained instruments: a scanning electron microscope (JEOL JSM-6510LV), an energy-dispersive X-ray spectroscopy detector (Thermo Scientific UltraDry), and a data acquisition computer

workstation with SEM (JEOL SEM Control User Interface 2.23) and EDS (Thermo Fisher Scientific Noran System Six (NSS) 3.0) software.

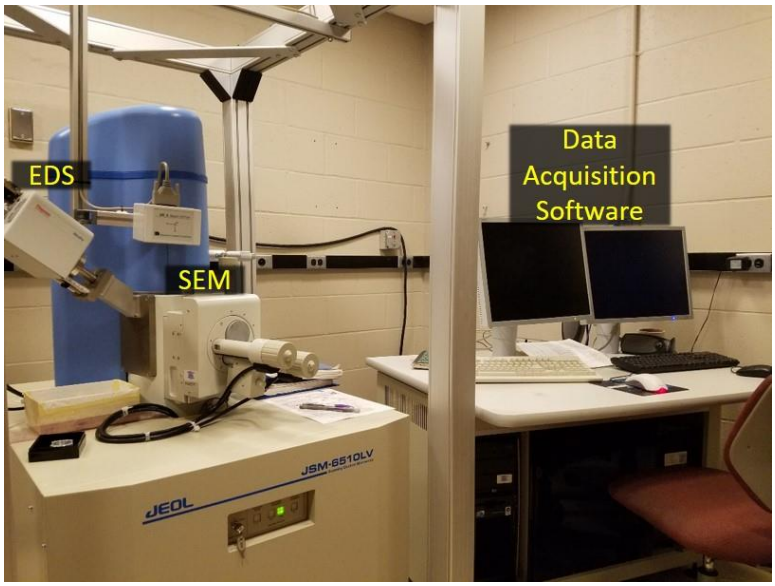

Figure 2.7: Laboratory setup for taking SEM/EDS data.

The SEM images were obtained by the collection of secondary electrons using an Everhart-Thornley detector. Secondary electrons were chosen due to their high topographical resolution and because there was not a need for the elemental contrast of backscattered electrons since EDS detection was used for elemental composition. Measurements were taken at room temperature and under vacuum of approximately 10 Pa. The electron beam was energized using a potential of 15 kV and focused on the sample at a working distance between 9 and 11 mm. The spot size parameter controlled a combination of the electron-probe diameter and the illumination current with values ranging from 99 (large diameter and current) to 1 (small diameter and current) – for this work it was set to 50. Whole inclusions were imaged with magnifications from 50X to

100X while individual spots were imaged with magnifications between 100X and 7000X depending on the structure being analyzed.

2.3.2 Data Acquisition and Analysis

Once quality SEM images were acquired, software was used to obtain elemental maps and X-ray spectra from the inclusions. The NSS software had peak identification techniques pre-programmed into the system so manual fitting was not needed. After the characteristic X-rays were detected, the software quantitatively tabulated the results with each element present classified by its percentage by weight.

3. Results and Data Analysis

In this chapter, the results of Raman spectroscopy and SEM/EDS are highlighted for both Moss and Murray. Raman results are represented with characteristic spectra, SEM results are displayed as images, and EDS results are shown with both element maps and tables containing element percentages by weight (wt. %) ranges.

3.1 Moss

3.1.1 Raman Spectroscopy

Figure 3.1 shows representative spectra obtained from various inclusions and spots in the Moss sample. Only high-resolution data are shown in this work as they gave clearer results, e.g. determination of doublet wavenumbers. For each spectrum, the main mineral is highlighted by the peaks that are labelled, with no labels on peaks coming from other minerals. Unless otherwise stated, peak identification and vibrational mode information can be found in Dall'Asén et al. (2017a, 2017b) and references therein.

The first spectrum (Fig. 3.1a) exhibits graphitic carbon peaks at ~1344 and 1602 cm^{-1}, which are termed D- and G-bands, respectively. The D-band results from defects in the crystal structure while the G-band comes from the stretching of C-C bonds. Magnesium-rich olivine, also known as forsterite (Mg_2SiO_4), is shown by the doublet with peaks of ~827 and 859 cm^{-1} (Fig. 3.1b). Here, the symmetric and antisymmetric stretching modes from Si-O bonds give rise to the identifying peaks. Enstatite ($MgSiO_3$), which is a form of Mg-rich pyroxene, is revealed with peaks at ~239, 334, 401, 663/684, and 1014/1035 cm^{-1} (Fig. 3.1c). The peaks are produced by the symmetrical stretching of both

the Si-O and Si-O-Si bonds. The last spectrum (Fig. 3.1d) displays peaks at ~223, 293, 403, 490, and 591 cm^{-1} for hematite (Fe_2O_3) and ~672 cm^{-1} for magnetite (Fe_3O_4). Hematite peaks come from Fe-O transverse optical modes while the magnetite peak originates from the symmetric stretching of the oxygen atoms in the Fe-O bonds (Lin et al. 2014). The usual ~1284 cm^{-1} peak of hematite is hidden due to the graphitic carbon also in the vicinity.

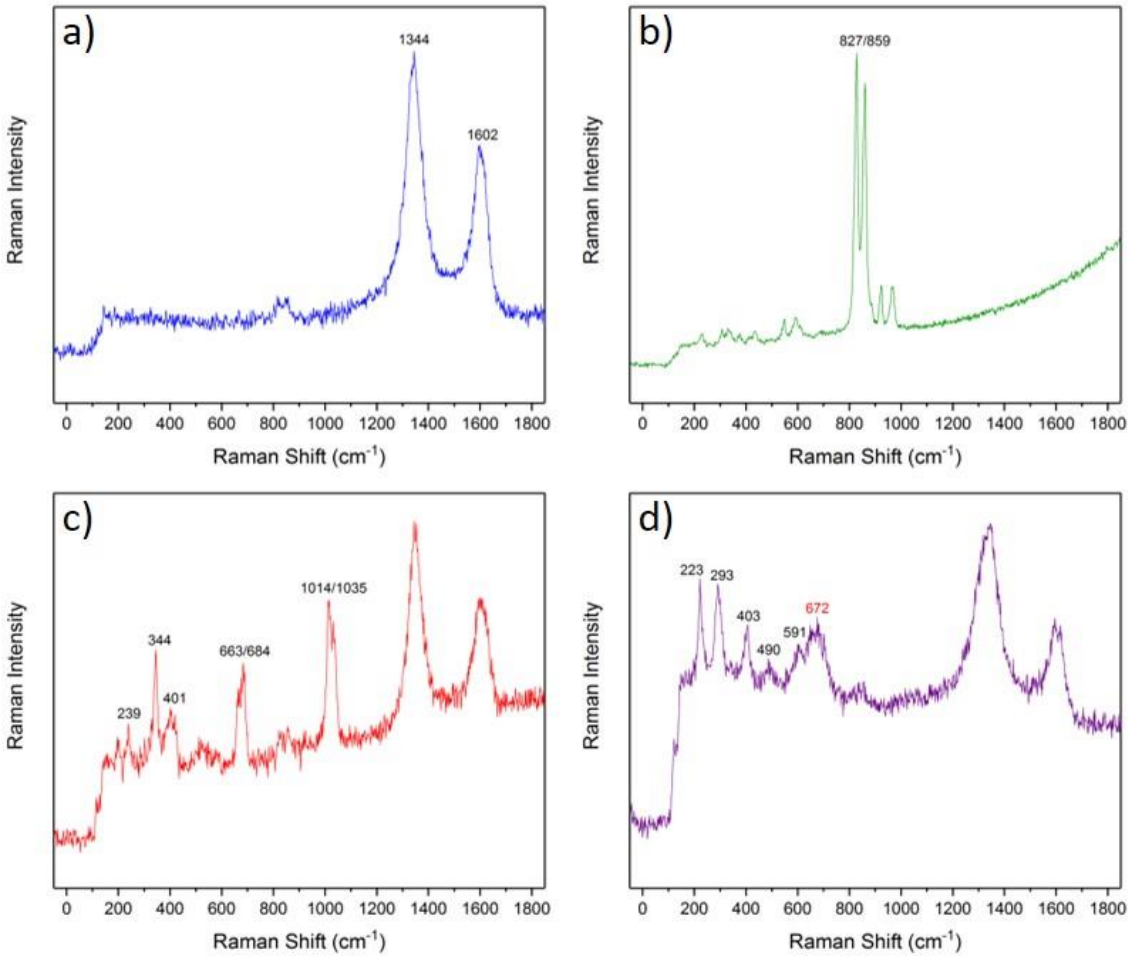

Figure 3.1: Representative Raman spectra of minerals found in Moss – only peaks corresponding to the respective mineral are labelled. a) Graphitic carbon from inclusion 7 spot 6; also a weak olivine signal. b) Forsterite (Mg-rich olivine) from inclusion 6 spot 2; also smaller, secondary olivine signals. c) Enstatite (Mg-rich pyroxene) from inclusion 11 spot 3; also graphitic carbon and weak olivine signals. d) Hematite (black numbers) and magnetite (red number) from inclusion 6 spot 4; also, a graphitic carbon signal which hides the ~1284 cm^{-1} peak from hematite.

The three inclusions studied with Raman spectroscopy in Moss contained graphitic carbon, forsterite, and enstatite inside the boundaries of the inclusions. The same minerals were found in the surrounding matrix of the inclusions along with the addition of hematite and magnetite.

3.1.2 SEM and EDS

Figures 3.2, 3.7, 3.11, 3.17, and 3.21 display SEM images and EDS maps of the well-defined inclusions and their respective matrix from the Moss sample. The secondary electron images show distinct boundaries between the inclusions and matrix (cracks, rims, or black-white contrast). These images also exhibit the different topography within the inclusions and throughout the matrix (i.e. the different shades of white and grey inside inclusion 6). Each of the figures also indicates the location of the spots used for taking higher resolution data and are marked with yellow numbers. The selected higher resolution SEM images and EDS maps (Figs. 3.3-3.6, 3.8-3.10, 3.12-3.16, 3.18-3.20, and 3.22-3.24) show interesting morphologies on scales of microns and tens of microns. In general, these unique structures also included distinct configurations or combinations of elements.

Overall, some correlations were commonly found throughout the inclusions and matrix. Inside the inclusions there was a higher relative concentration of Mg, Si, and O than in the matrix. Iron-sulfur surrounded the inclusions (either as rims, in veins, or in the matrix; Figs. 3.2, 3.7, 3.10, 3.11, and 3.21) and occasionally there were some clusters of Fe-Ni (Figs. 3.6, 3.12, 3.14, and 3.18). Iron was more prominent in the matrix than in the inclusions and where Fe was present, Mg and Si were absent. Occasionally, patches of

Al-Ca and/or Al-Ca-Na were found in both the inclusions and the matrix (Figs. 3.3, 3.10, 3.16, and 3.18). Carbon was generally found in small areas scattered throughout the meteorite. Upon further investigation at higher resolutions, C was mainly in the form of smooth structures up to about 10 to 20 microns in size (Figs. 3.5, 3.8, 3.9, 3.10, 3.15, 3.16, 3.19, 3.20, 3.23, and 3.24).

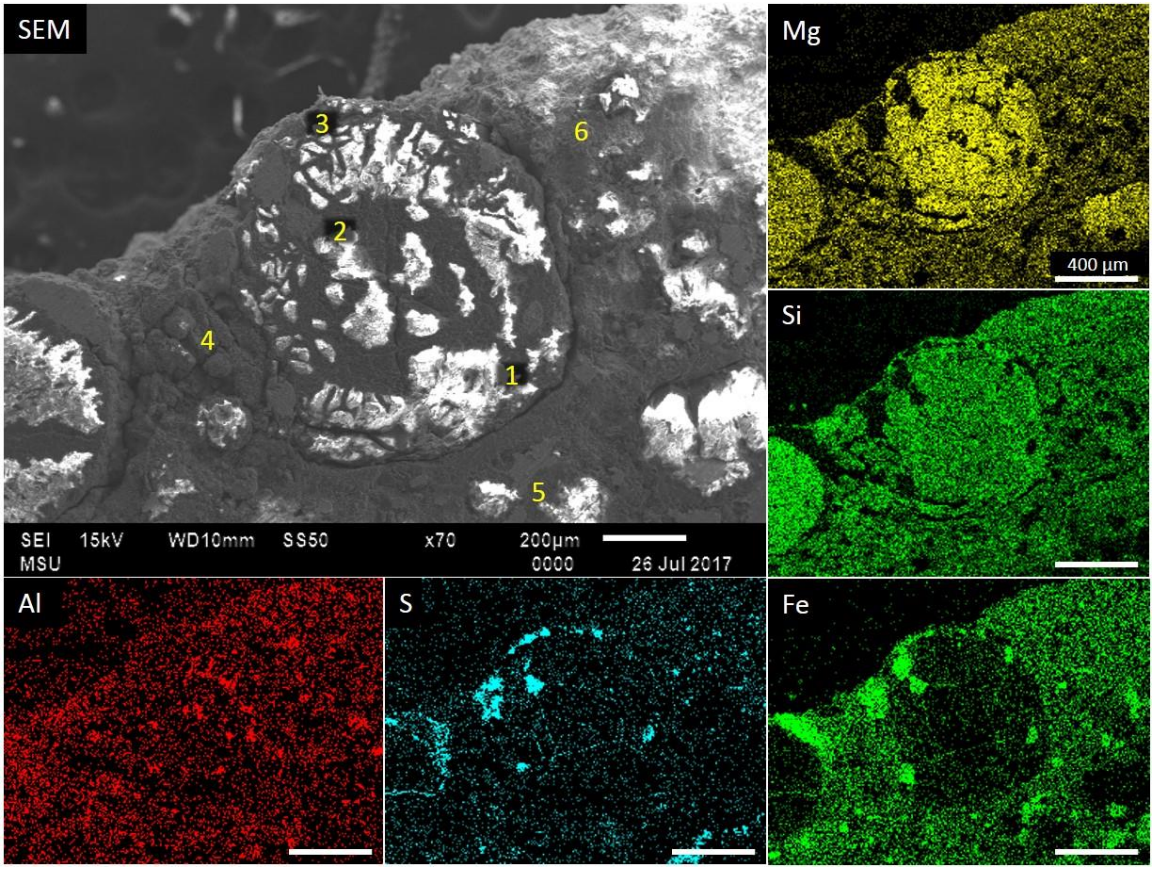

Figure 3.2: SEM image and EDS maps of inclusion 6 and surrounding matrix in Moss at 70X magnification. SEM image shows the topography of the well-defined inclusion and adjacent matrix. Yellow numbers in the SEM image indicate the locations of spots used for higher magnification data. EDS maps show correlations between Mg-Si and Fe-S (note the patches throughout the inclusion) as well as some patches of Al.

Table 3.1 gives the percentage by weight ranges retrieved from the data of whole inclusion views in Moss (Figs. 3.2, 3.7, 3.11, 3.17, and 3.21) and the bulk mean composition for CO chondrites from Hutchison (2004). Even with the differing inclusion

sizes and magnifications used for imaging, the relative abundance of elements kept the same order. The major elements were O, Fe, Si, and Mg; the minor elements were C, Ca, Ni, S, and Al; and the trace elements were Na and Cr.

Moss CO3.6 Meteorite											
Element (wt. %)	O	Fe	Si	Mg	C	Ca	Ni	S	Al	Na	Cr
This Study	32.0-34.5	23.0-30.0	15.0-17.5	13.0-14.0	2.0-3.0	2.0-3.0	1.0-2.0	1.0-2.0	1.0-2.0	0.5-1.0	0.5-1.0
Hutchison 2004	36.5	24.8	15.9	14.5	0.5	1.6	1.4	2.0	1.4	0.4	0.4

Table 3.1: Element wt. % range for whole inclusions and surrounding matrix in Moss obtained in this study and the bulk mean composition for CO chondrites reported in Hutchison 2004.

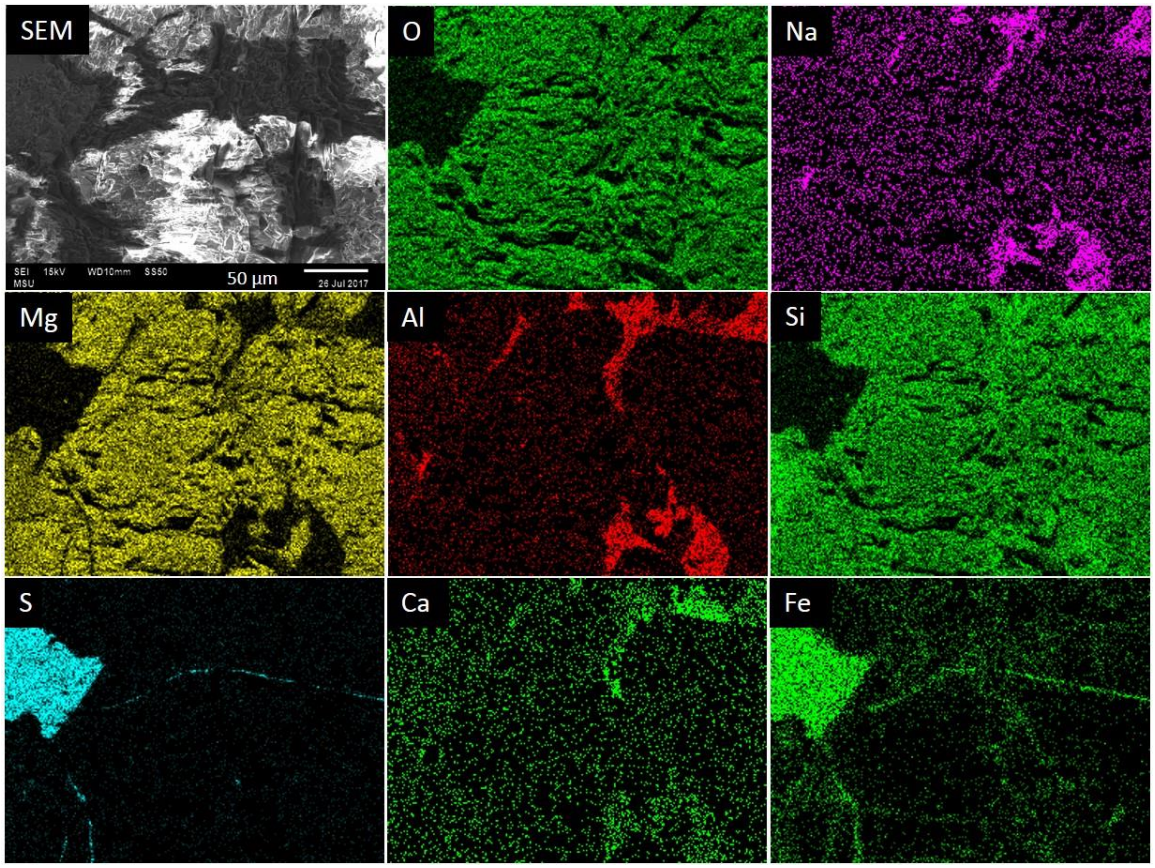

Figure 3.3: SEM image and EDS maps of spot 2 of inclusion 6 (marked in Fig. 3.2) in Moss at 430X magnification. EDS maps show correlations between Mg-Si-O, Al-Ca-Na, and Fe-S.

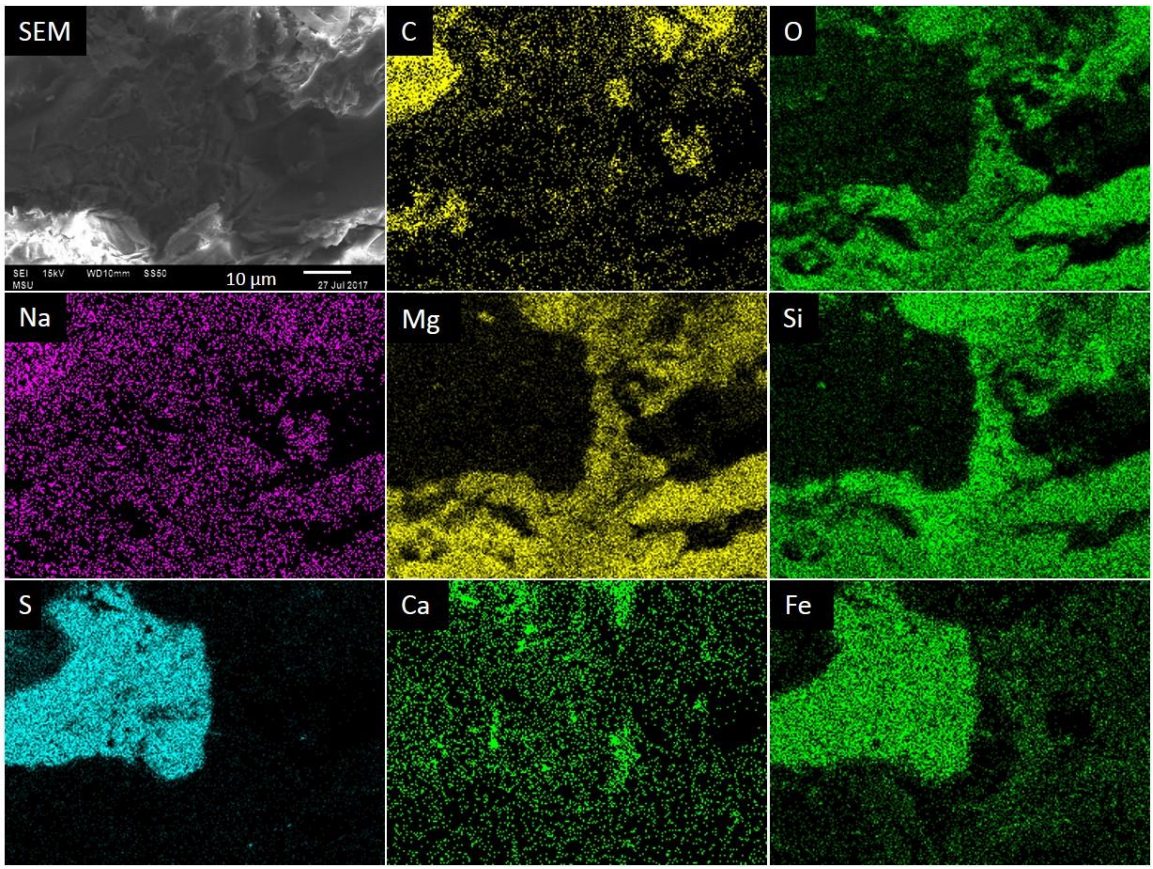

Figure 3.4: SEM image and EDS maps of spot 3 of inclusion 6 (marked in Fig. 3.2) in Moss at 1600X magnification. EDS maps show correlations between Mg-Si-O and Fe-S as well as patches of C, Na, and Ca.

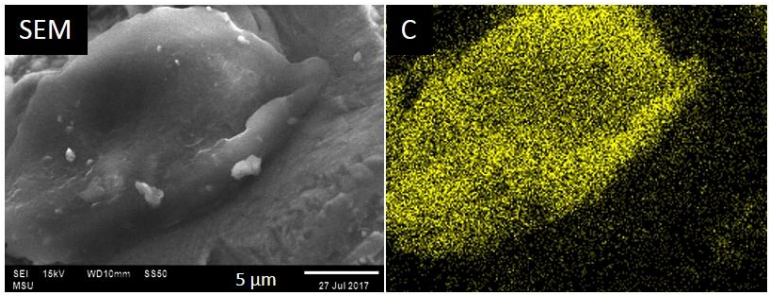

Figure 3.5: SEM image and EDS map of spot 3 of inclusion 6 (marked in Fig. 3.2) in Moss at 5000X magnification. SEM image shows a smooth, ~10 µm sized structure corresponding to C in the EDS map.

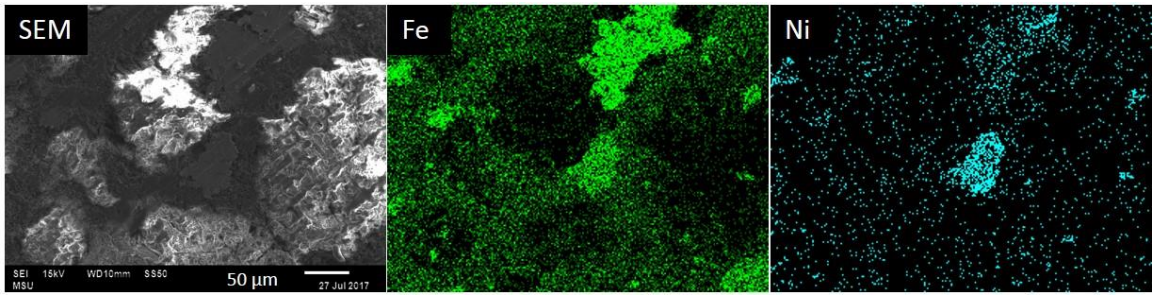

Figure 3.6: SEM image and EDS maps of spot 5 of inclusion 6 (marked in Fig. 3.2) in Moss at 300X magnification. EDS maps show a correlation between Fe-Ni.

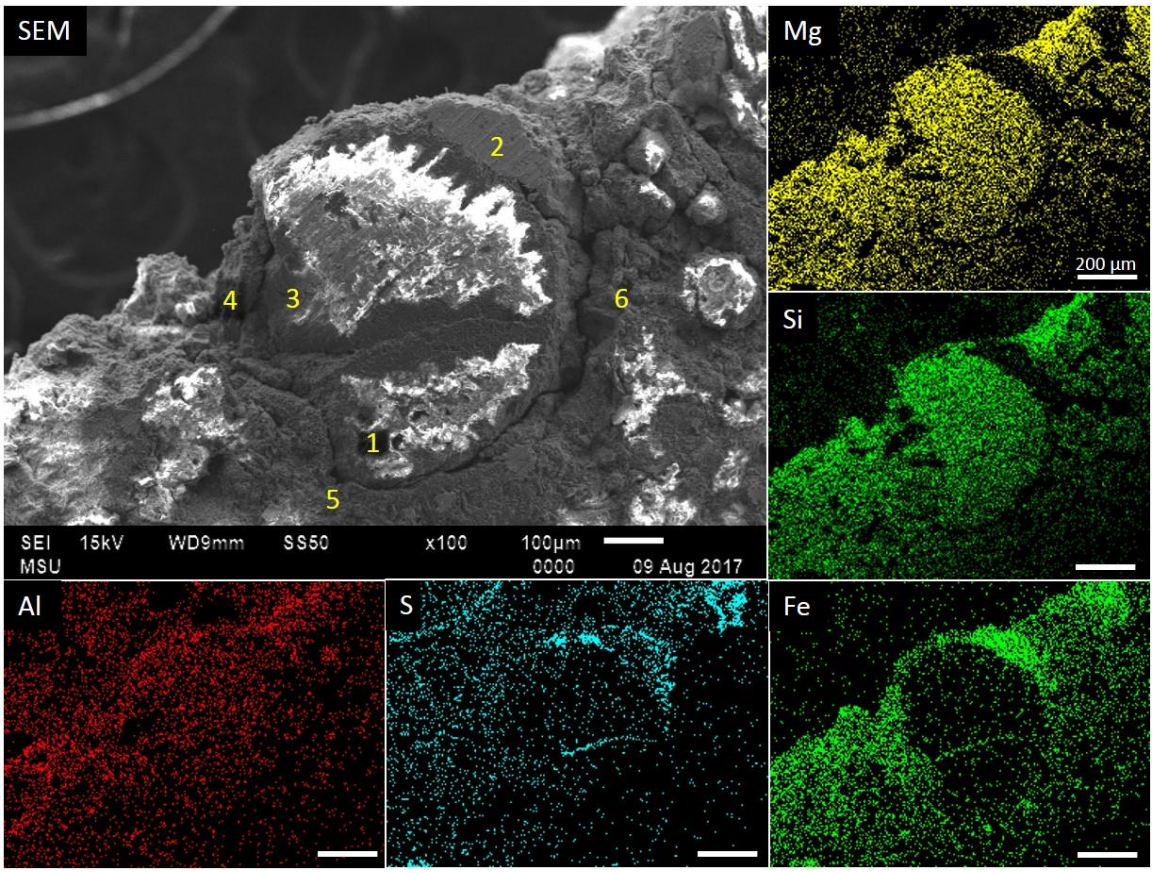

Figure 3.7: SEM image and EDS maps of inclusion 7 and surrounding matrix in Moss at 100X magnification. SEM image shows the topography of the well-defined inclusion and adjacent matrix. Yellow numbers in the SEM image indicate the locations of spots used for higher magnification data. EDS maps show correlations between Mg-Si and Fe-S (note the patches/half-rim on the upper right of the inclusion) as well as some patches of Al.

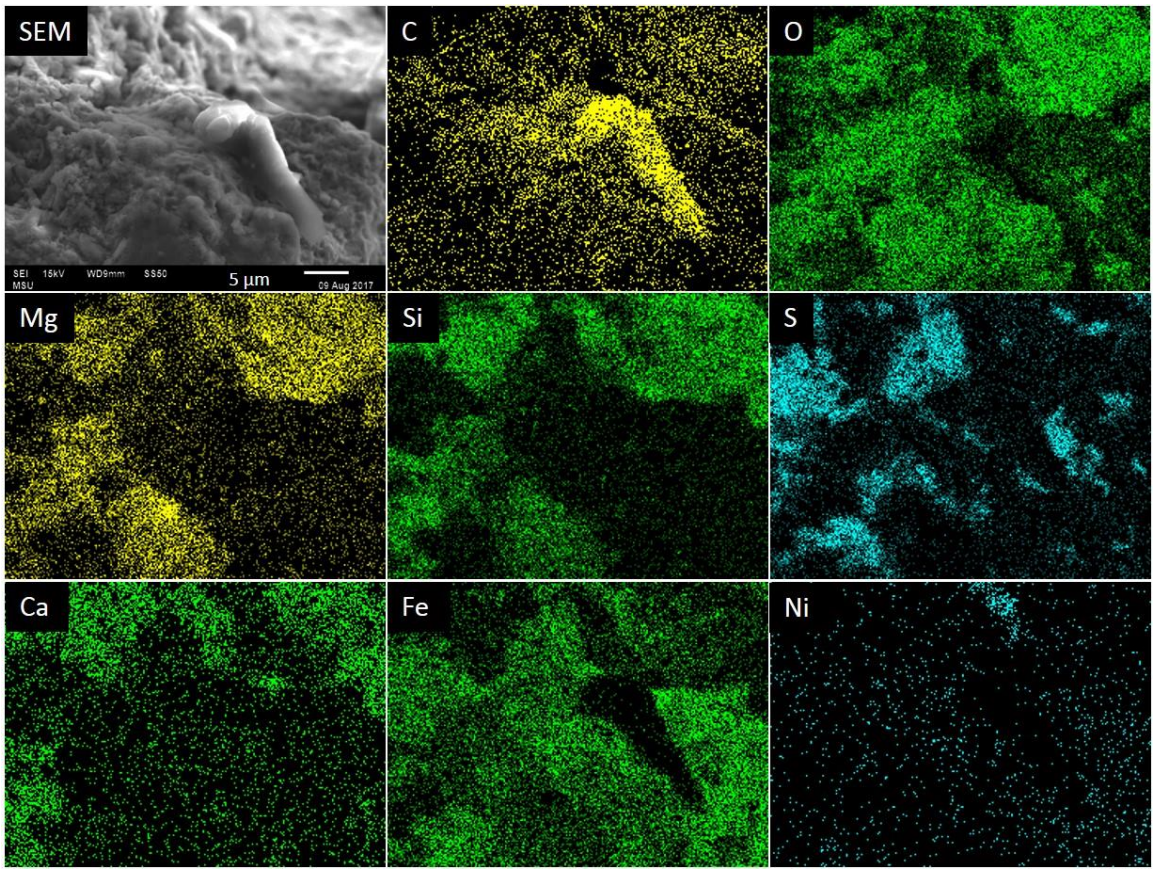

Figure 3.8: SEM image represents spot 2 of inclusion 7 (marked in Fig. 3.7) in Moss at 3000X magnification. EDS maps show correlations between Mg-Si-O-Ca and Fe-S-O, a patch of Ni, and a smooth, ~10 µm sized structure of C.

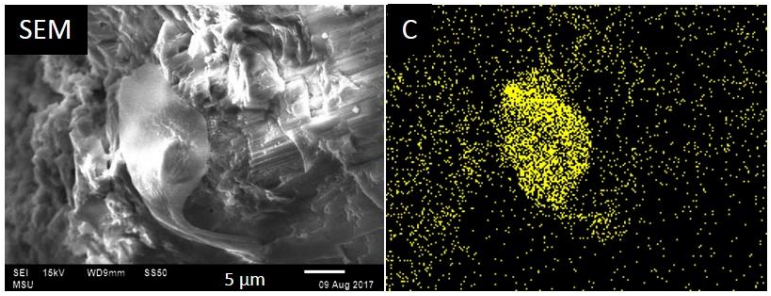

Figure 3.9: SEM image and EDS map of spot 3 of inclusion 7 (marked in Fig. 3.7) in Moss at 2700X magnification. SEM image shows a smooth, ~10 µm sized structure corresponding to C in the EDS map.

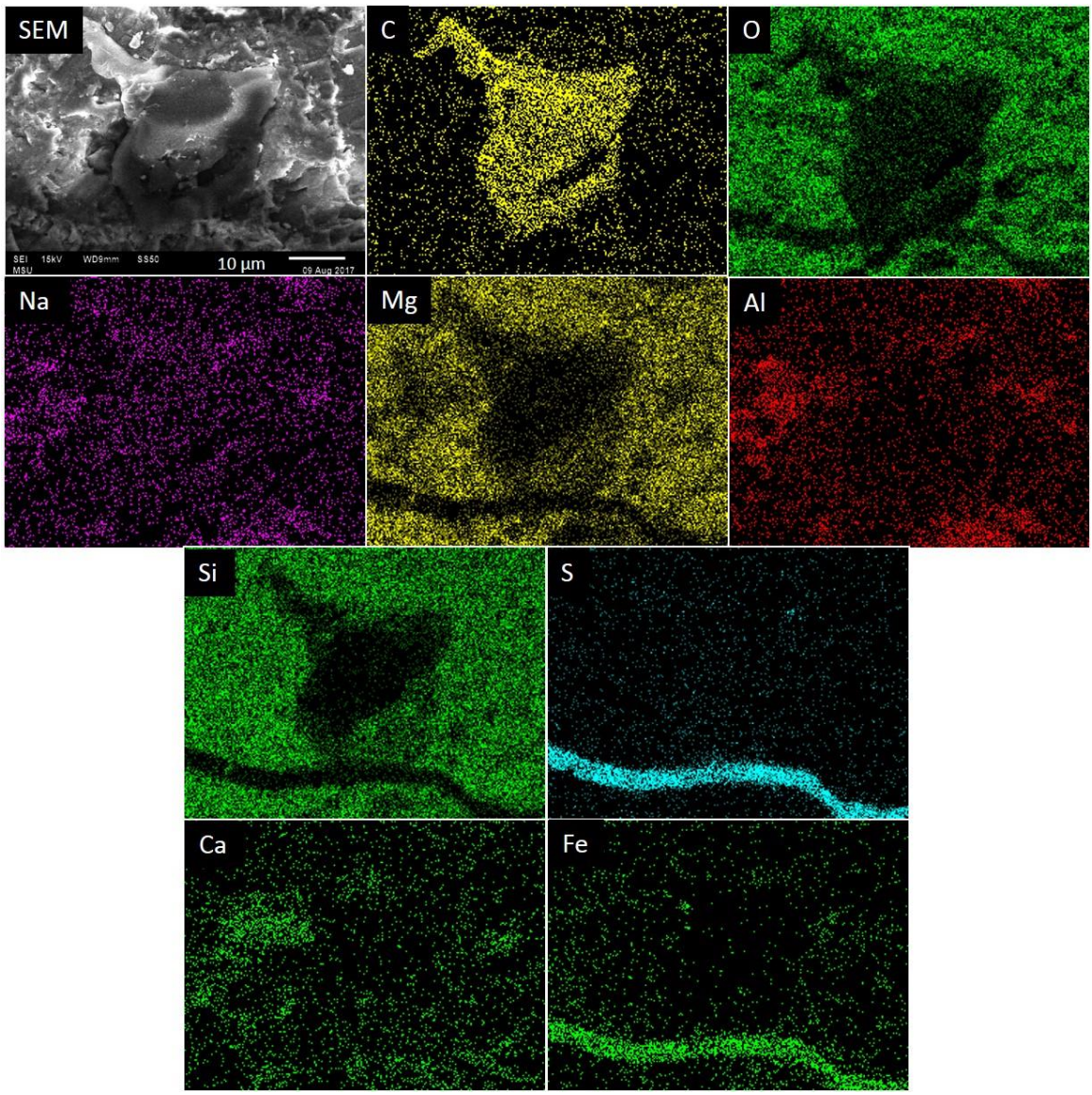

Figure 3.10: SEM image and EDS maps of spot 6 of inclusion 7 (marked in Fig. 3.7) in Moss at 2000X magnification. SEM image shows a smooth, ~10 µm sized structure corresponding to C in the EDS map. EDS maps also show correlations between Mg-Si-O, Al-Ca-Na, and Fe-S (note the vein running through the middle of the inclusion).

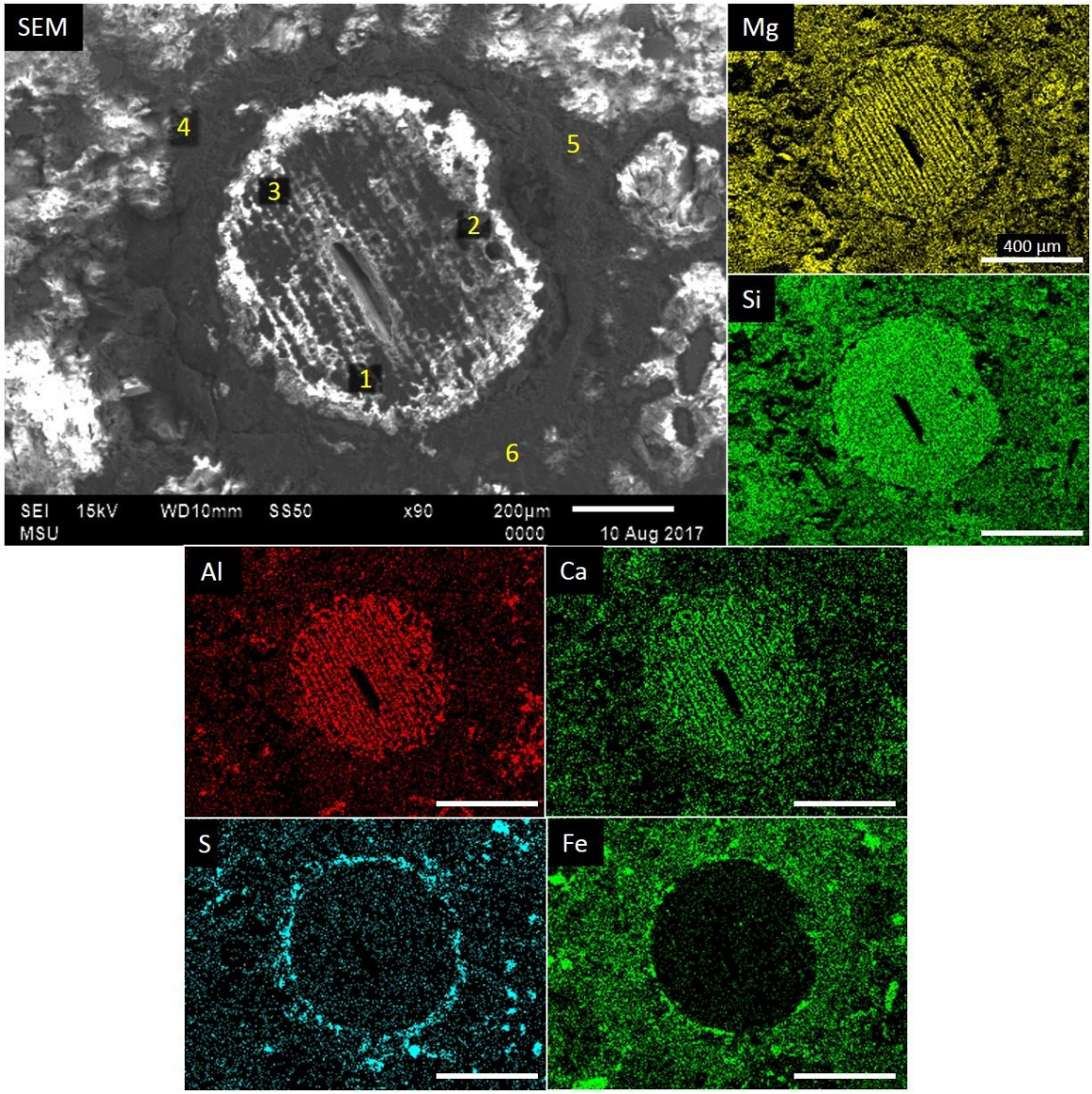

Figure 3.11: SEM image and EDS maps of inclusion 11 and surrounding matrix in Moss at 90X magnification. SEM image shows the topography of the well-defined inclusion and adjacent matrix. Yellow numbers in the SEM image indicate the locations of spots used for higher magnification data. EDS maps show correlations between Mg-Si, Al-Ca, and Fe-S (note the rim surrounding the inclusion).

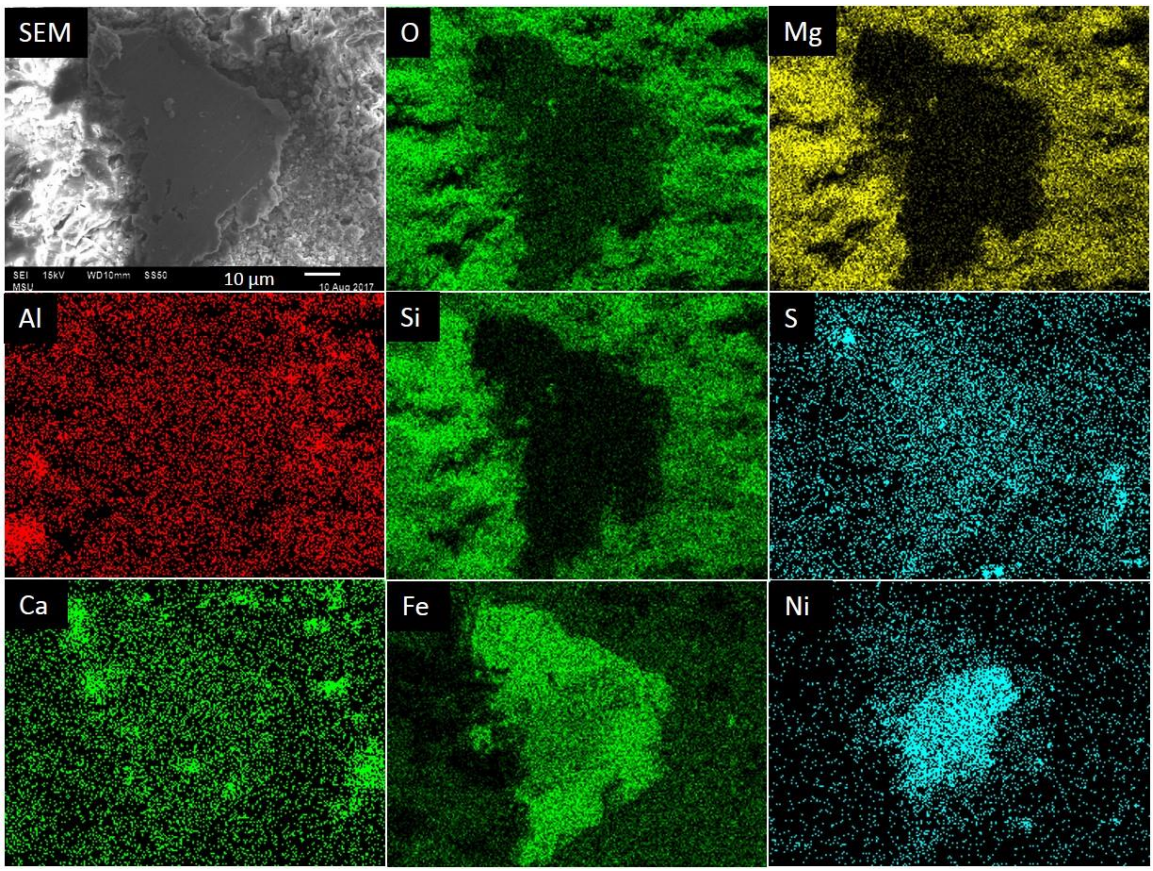

Figure 3.12: SEM image and EDS maps of spot 4 of inclusion 11 (marked in Fig. 3.11) in Moss at 1200X magnification. EDS maps show correlations between Mg-Si-O, Fe-S, and Fe-Ni as well as patches of Al and Ca.

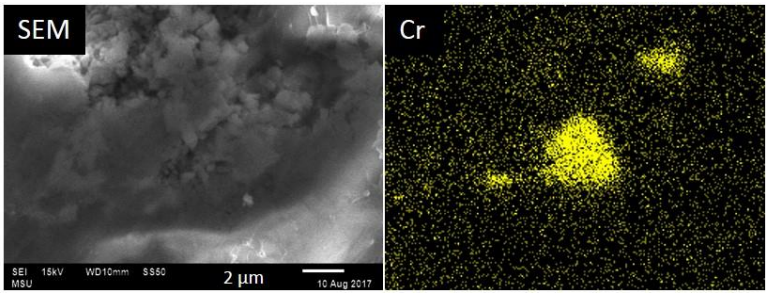

Figure 3.13: SEM image and EDS map of spot 4 of inclusion 11 (marked in Fig. 3.11) in Moss at 7000X magnification. EDS map shows a few Cr patches of approximately micron size.

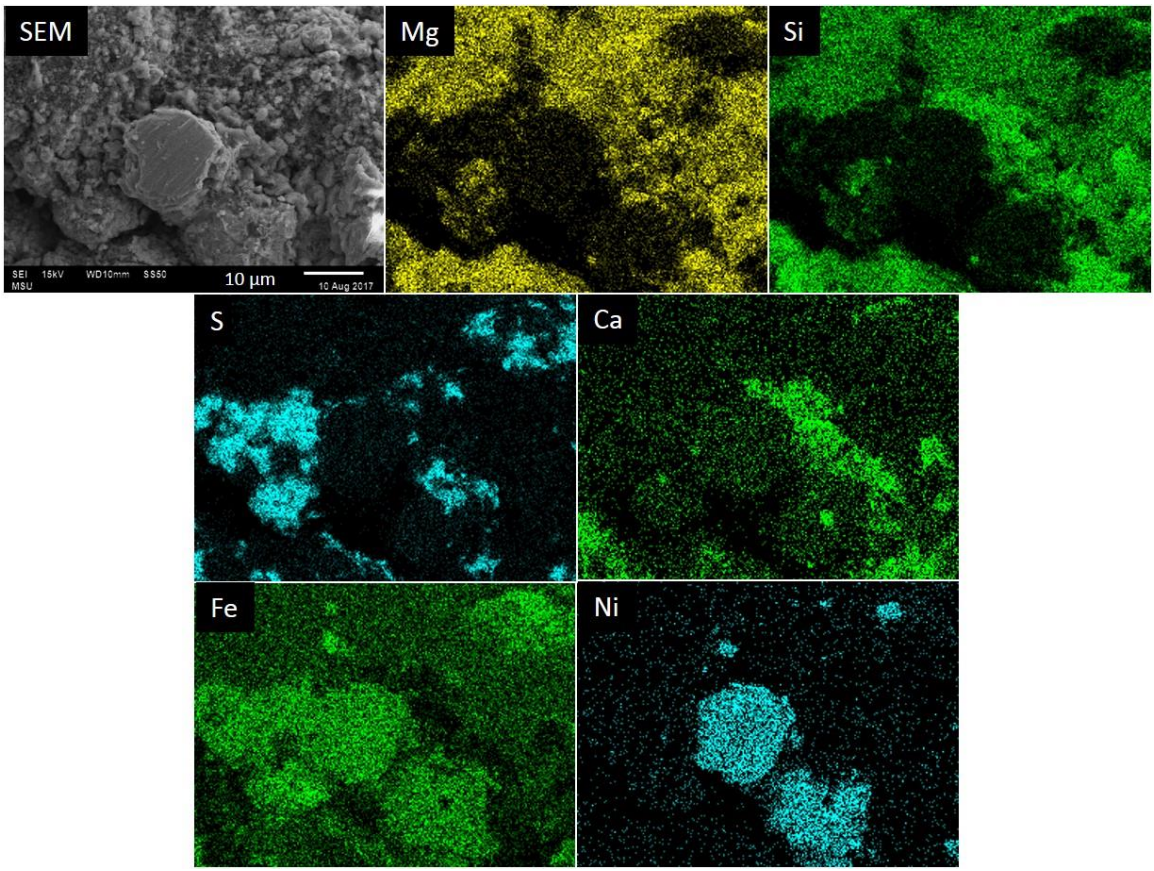

Figure 3.14: SEM image and EDS maps of spot 5 of inclusion 11 (marked in Fig. 3.11) in Moss at 2000X magnification. EDS maps show correlations between Mg-Si, Ca-Si, Fe-S, and Fe-Ni.

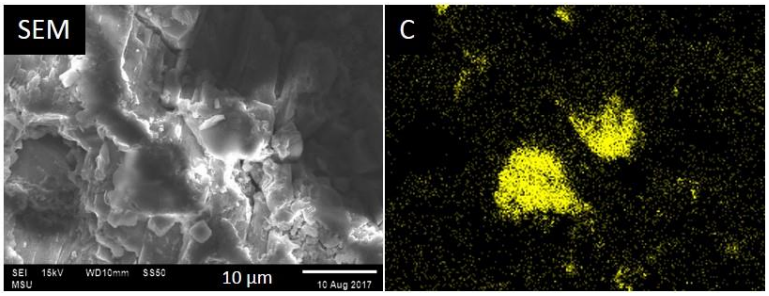

Figure 3.15: SEM image and EDS map of spot 6 of inclusion 11 (marked in Fig. 3.11) in Moss at 2500X magnification. SEM image shows two smooth, ~10 µm sized structures corresponding to C in the EDS map.

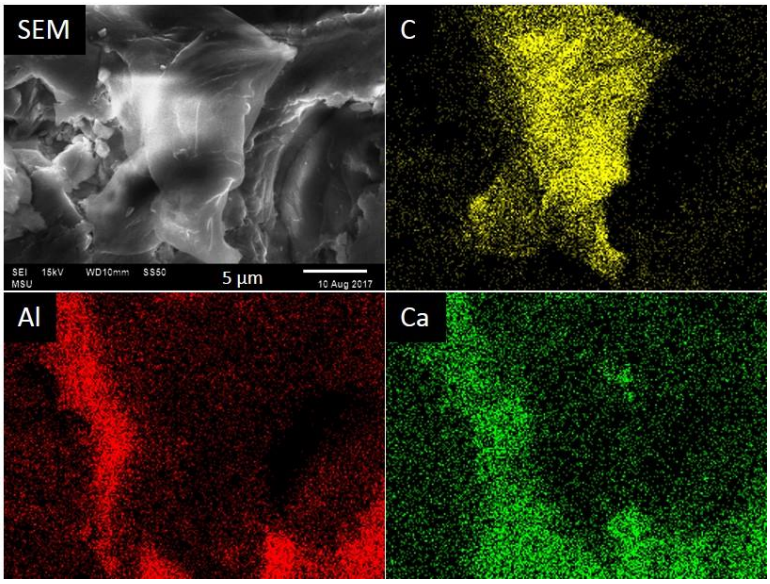

Figure 3.16: SEM image and EDS maps of spot 6 of inclusion 11 (marked in Fig. 3.11) in Moss at 4300X magnification. SEM image shows a smooth, ~10 µm sized structure corresponding to C in the EDS map. EDS maps also show a correlation between Al-Ca.

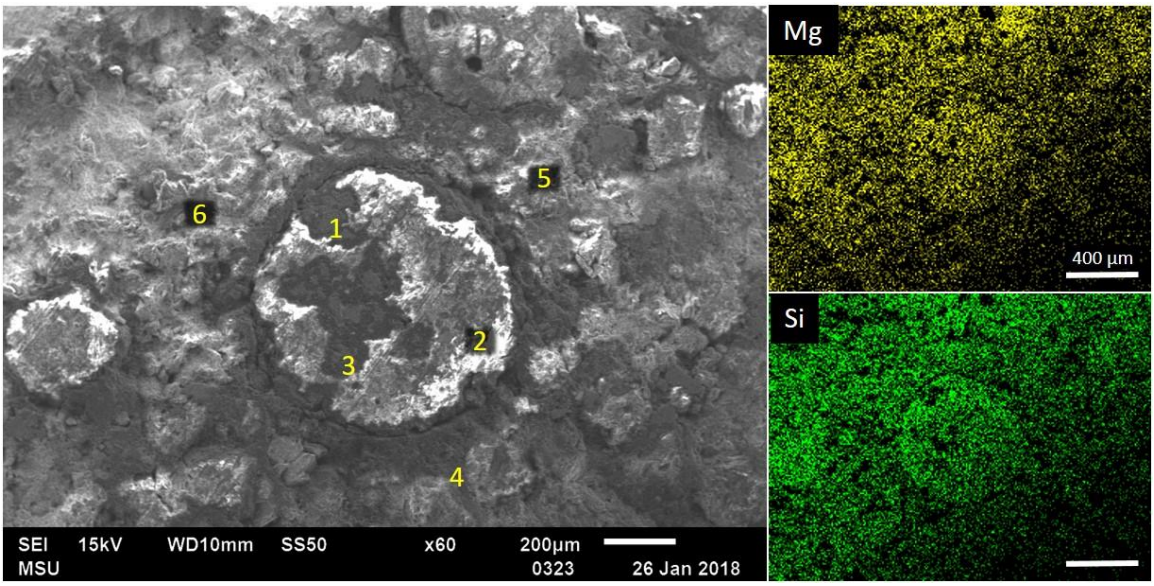

Figure 3.17: SEM image and EDS maps of inclusion 12 and surrounding matrix in Moss at 60X magnification. SEM image shows the topography of the well-defined inclusion and adjacent matrix. Yellow numbers in the SEM image indicate the locations of spots used for higher magnification data. EDS maps show a correlation between Mg-Si.

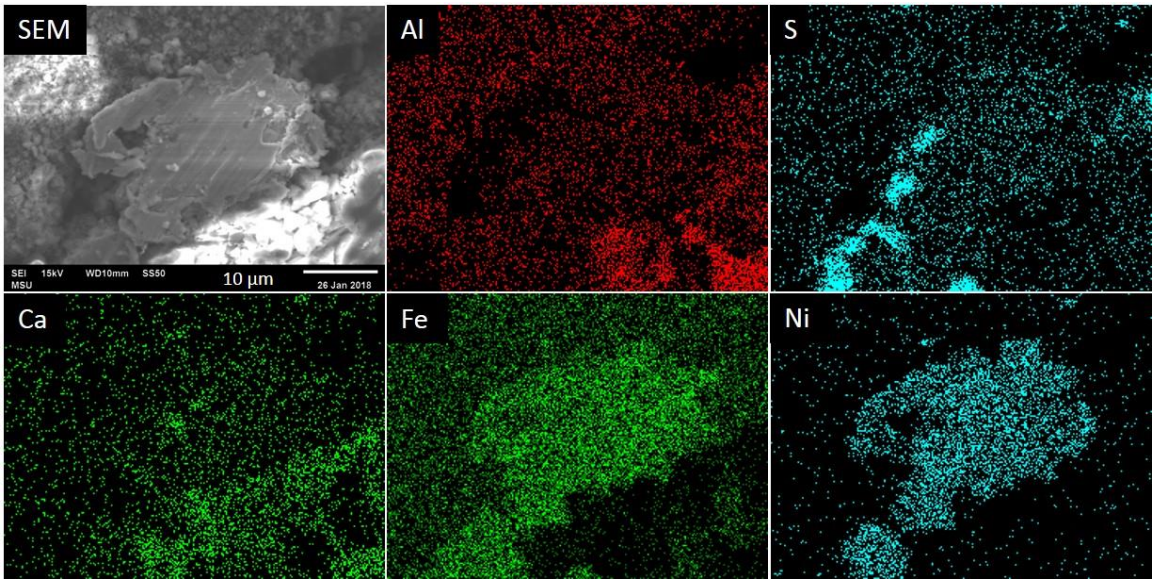

Figure 3.18: SEM image and EDS maps of 1 of inclusion 12 (marked in Fig. 3.17) in Moss at 2500X magnification. EDS maps show correlations between Al-Ca and Fe-Ni as well as patches of S.

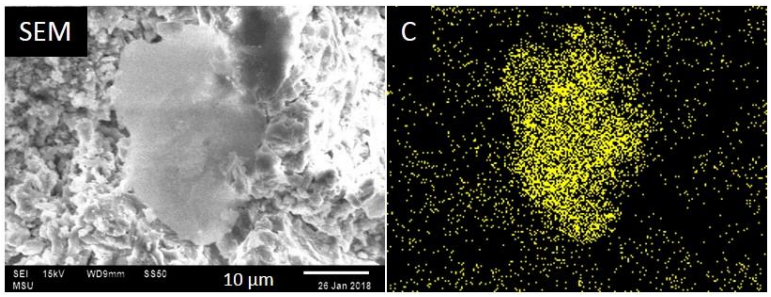

Figure 3.19: SEM image and EDS map of spot 4 of inclusion 12 (marked in Fig. 3.17) in Moss at 2200X magnification. SEM image shows a smooth, ~10 µm sized structure corresponding to C in the EDS map.

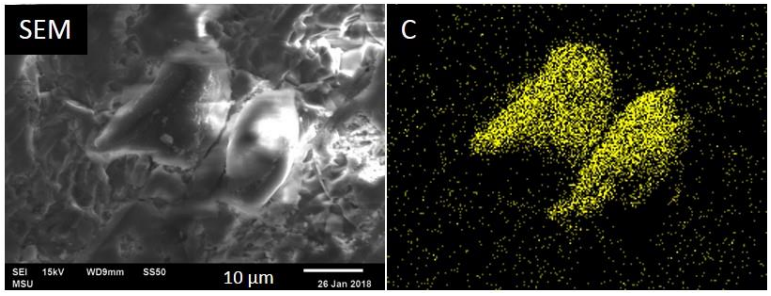

Figure 3.20: SEM image and EDS map of spot 5 of inclusion 12 (marked in Fig. 3.17) in Moss at 2000X magnification. SEM image shows two smooth, ~10 µm sized structures corresponding to C in the EDS map.

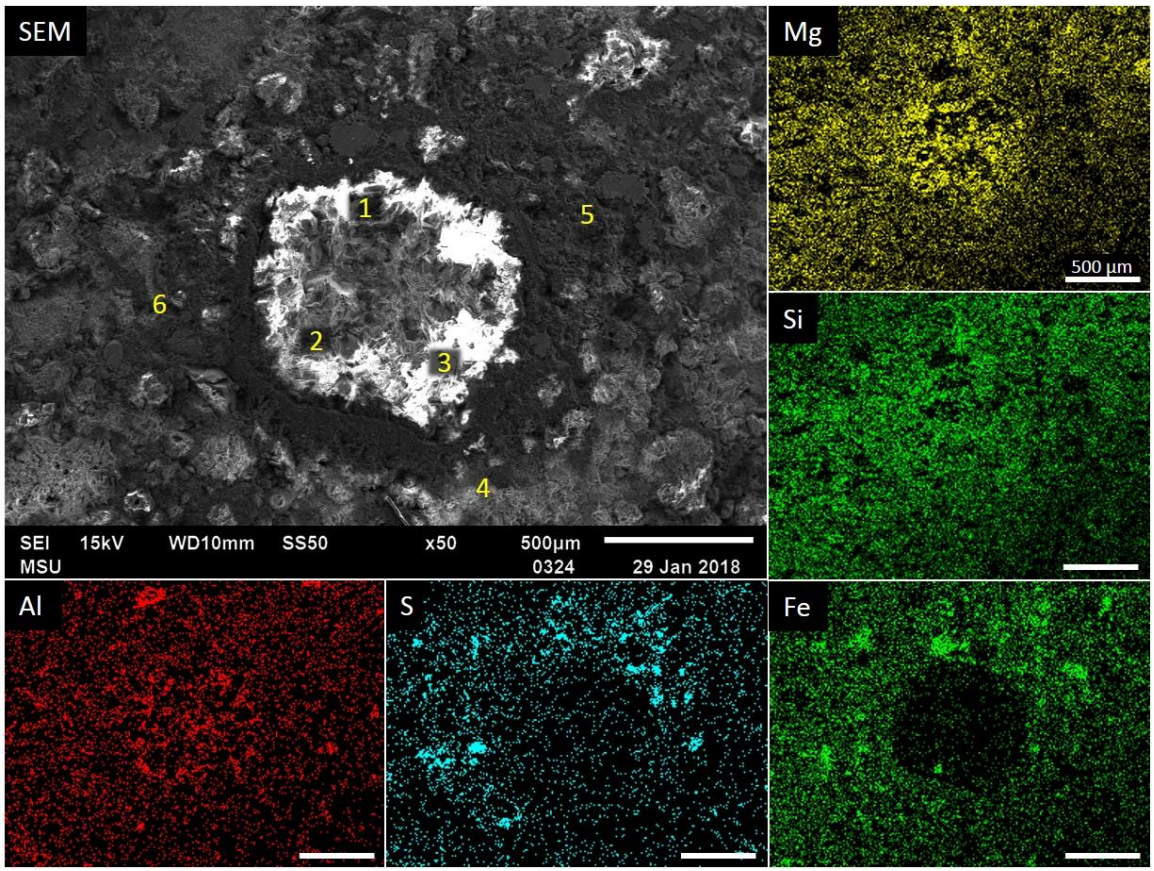

Figure 3.21: SEM image and EDS maps of inclusion 13 and surrounding matrix in Moss at 50X magnification. SEM image shows the topography of the well-defined inclusion and adjacent matrix. Yellow numbers in the SEM image indicate the locations of spots used for higher magnification data. EDS maps show correlations between Mg-Si and Fe-S as well as patches of Al.

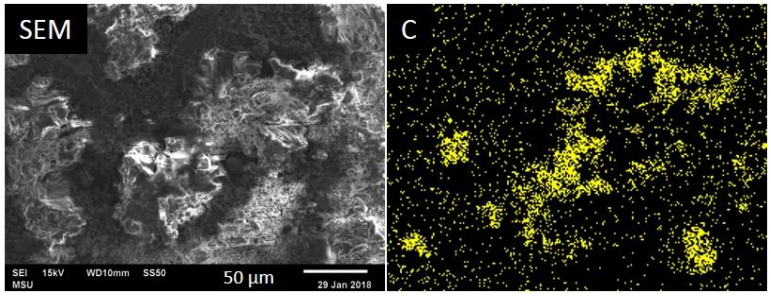

Figure 3.22: SEM image and EDS map of spot 4 of inclusion 13 (marked in Fig. 3.21) in Moss at 430X magnification. EDS map shows patches of C.

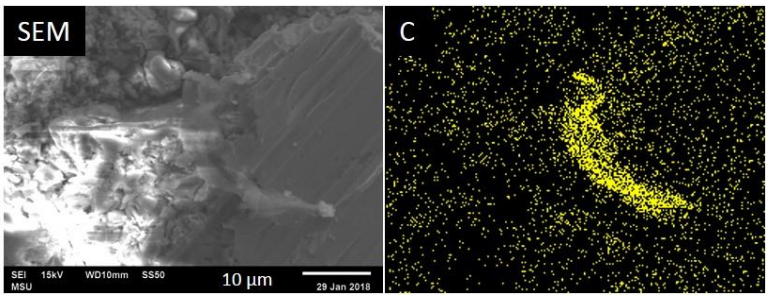

Figure 3.23: SEM image and EDS map of spot 5 of inclusion 13 (marked in Fig. 3.21) in Moss at 2300X magnification. SEM image shows a smooth, ~10 µm sized structure corresponding to C in the EDS map.

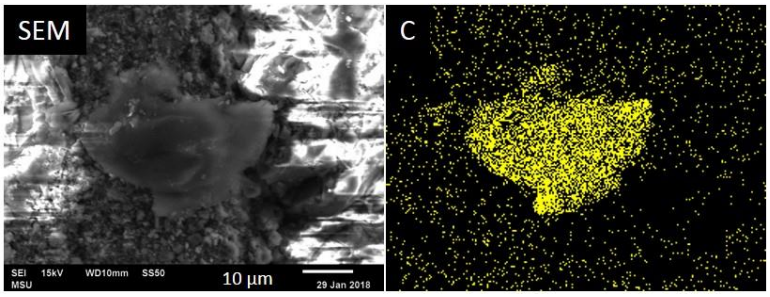

Figure 3.24: SEM image and EDS map of spot 6 of inclusion 13 (marked in Fig. 3.21) in Moss at 1700X magnification. SEM image shows a smooth, ~20 µm sized structure corresponding to C in the EDS map.

3.2 Murray

3.2.1 Raman Spectroscopy

Figure 3.25 shows examples of some high-resolution spectra acquired from various inclusions and spots in the Murray sample. The peak labelling procedures and the sources used for mineral identification are the same as those used for the Moss sample (Section 3.1.1). As in Moss, graphitic carbon, Mg-rich olivine (forsterite), and Mg-rich pyroxene (enstatite) were found in Murray. In addition, other spectra were obtained corresponding to minerals that have not been identified yet. Figure 3.25d shows a spectrum of one of them displaying peaks at ~444 and 621 cm^{-1}, a second unknown mineral (or a

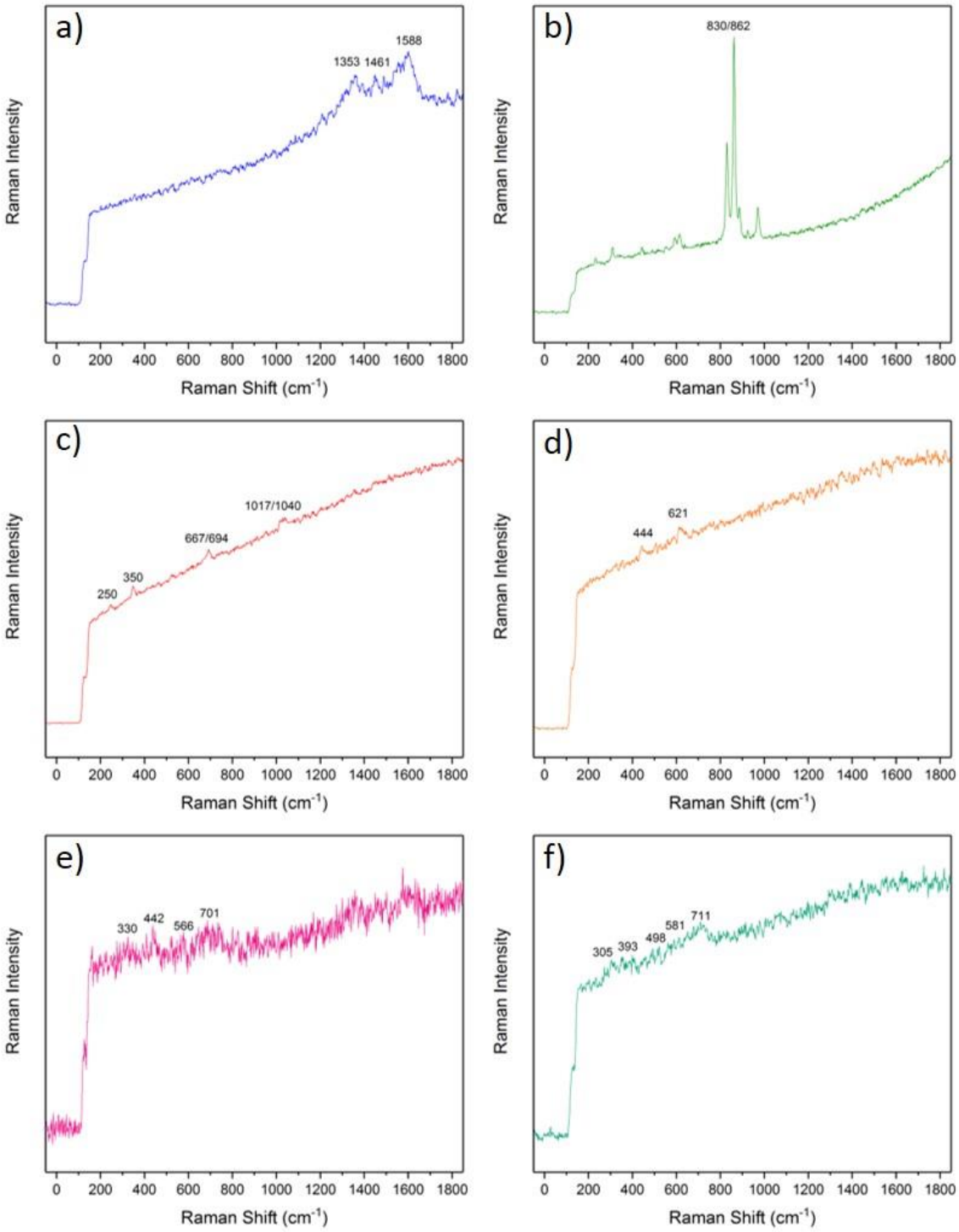

Figure 3.25: Representative Raman spectra of minerals found in Murray – only peaks corresponding to the respective mineral are labelled. a) Graphitic carbon from inclusion 6 spot 6. b) Forsterite (Mg-rich olivine) from inclusion 6 spot 1; also smaller, secondary olivine signals. c) Enstatite (Mg-rich pyroxene) from inclusion 2 spot 5. d) Unknown mineral from chondule 2 spot 6. e) Unknown mineral from inclusion 2 spot 3; also a graphitic carbon signal. f) Unknown mineral from distinct orange spot located in the matrix between inclusions 4 and 5.

combination of minerals) has peaks at ~330, 442, 566, and 701 cm^{-1} (Fig. 3.25e), and a third unknown mineral (or combination of minerals) has peaks at ~305, 393, 498, 580, and 711 cm^{-1} (Fig. 3.25f).

The six inclusions studied with Raman spectroscopy in Murray contained almost exclusively forsterite inside the boundaries of the inclusions along with minimal enstatite and a minimum of two unidentified minerals. In the matrix, primarily graphitic carbon was found along with one or more unidentified mineral(s).

3.2.2 SEM and EDS

Figures 3.26, 3.28, 3.31, 3.32, 3.36, and 3.37 show SEM images and EDS maps of the well-defined inclusions and their respective matrix from the Murray sample. The secondary electron images show distinct borders (seen as different textures) between the

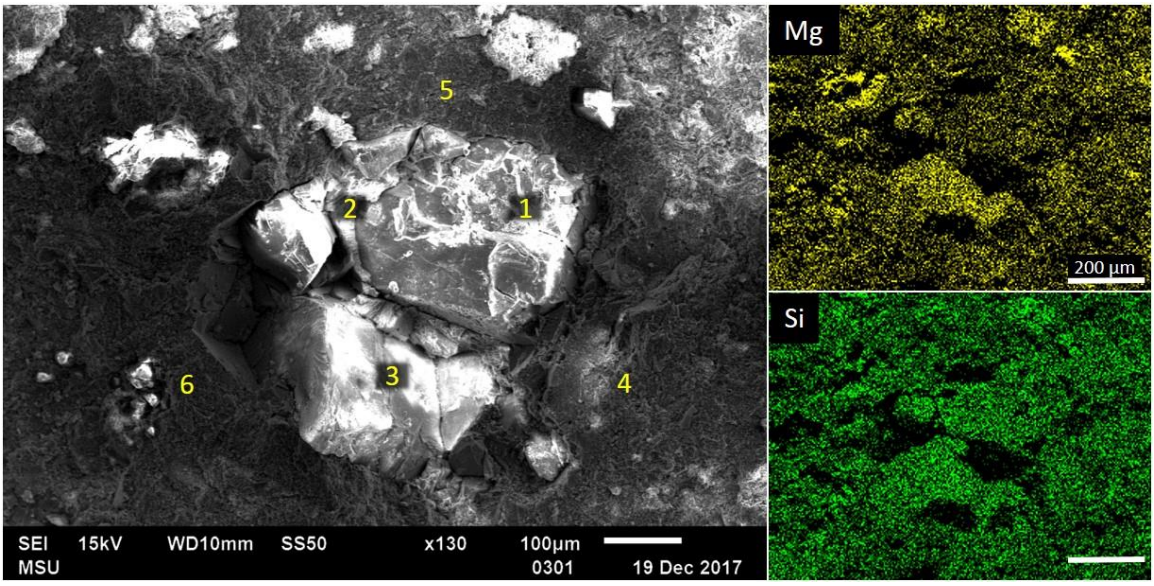

Figure 3.26: SEM image and EDS maps of inclusion 1 and surrounding matrix in Murray at 130X magnification. SEM image shows the topography of the well-defined inclusion and adjacent matrix. Yellow numbers in the SEM image indicate the locations of spots used for higher magnification data. EDS maps show a correlation between Mg-Si.

inclusions and matrix. These images also exhibit the different topography within the inclusions and throughout the matrix (e.g. the white spots that define inclusion 5 shown in Fig. 3.36). Each of the figures also indicates the location of the spots used for taking higher resolution data and are marked with yellow numbers. The selected higher resolution SEM images and EDS maps (Figs. 3.27, 3.29, 3.30, 3.33-3.35, 3.38, and 3.39) display diverse structures that range in size from microns to tens of microns. In general, these morphologies also included distinct arrangements or combinations of elements.

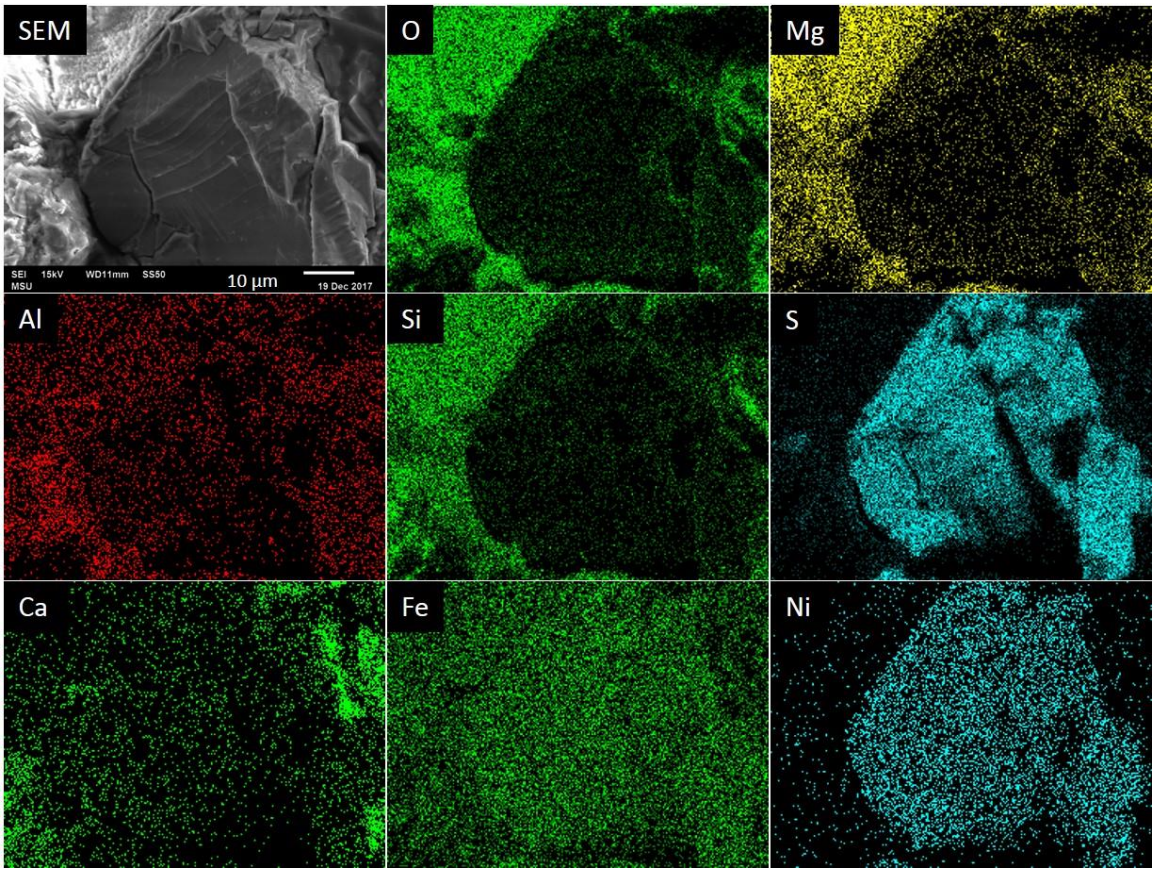

Figure 3.27: SEM image and EDS maps of spot 3 of inclusion 1 (marked in Fig. 3.26) in Murray at 1700X magnification. EDS maps show correlations between Mg-Si-O, Al-Ca, and Fe-S-Ni.

Overall, some connections were commonly found throughout the inclusions and matrix. Inside the inclusions there was a higher relative concentration of Mg-Si-O and in the matrix there was more Fe. Similar to Moss, where Fe-S or Fe-Ni were present both Mg and Si were absent (Figs. 3.27. 3.28, 3.31, 3.33, 3.36, and 3.37). Patches of Al-Ca and/or

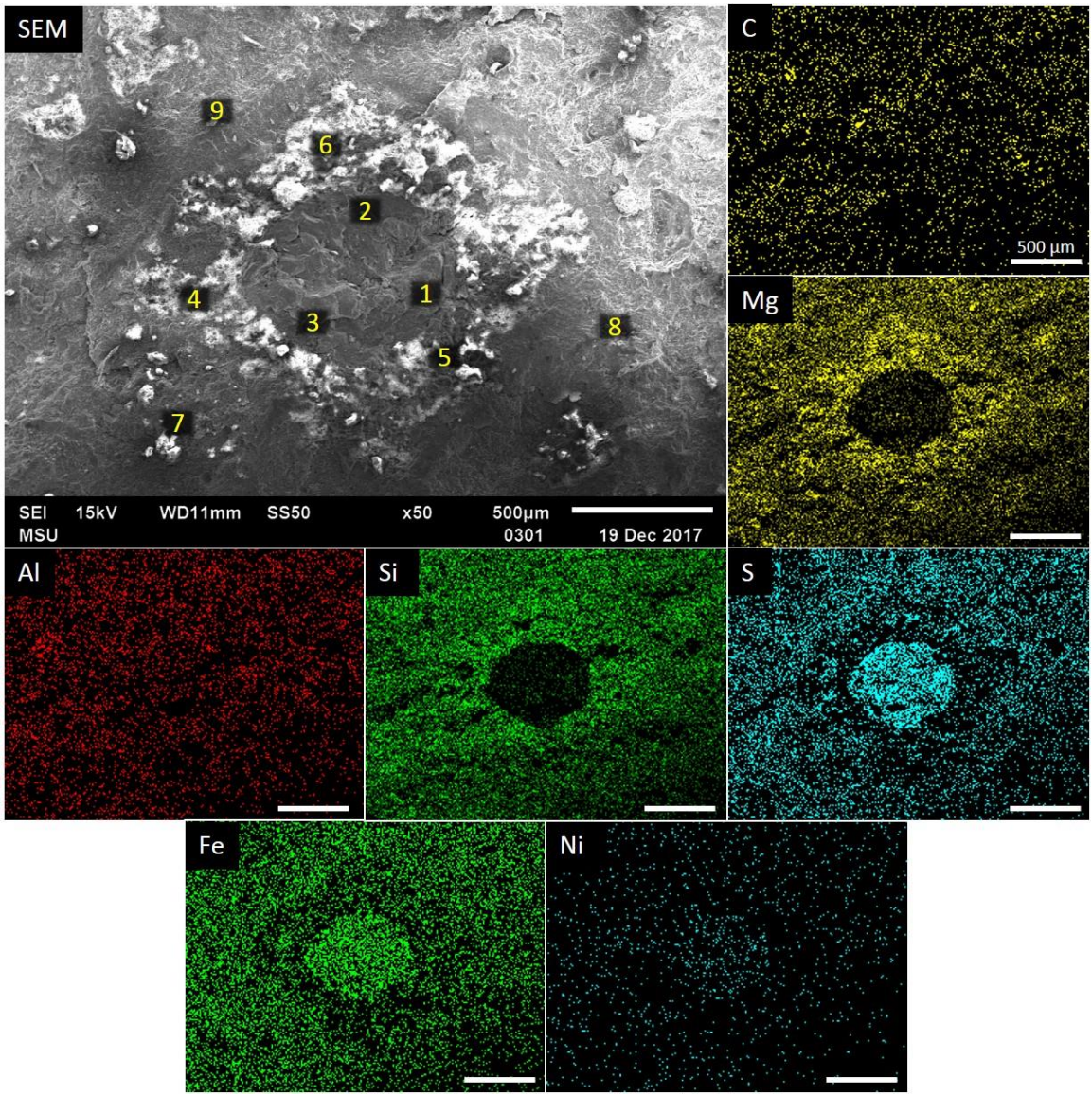

Figure 3.28: SEM image and EDS maps of inclusion 2 and surrounding matrix in Murray at 50X magnification. SEM image shows the topography of the well-defined inclusion and adjacent matrix. Yellow numbers in the SEM image indicate the locations of spots used for higher magnification data. EDS maps show a correlation between Mg-Si, Fe-S (note the chondrule-like center), and Fe-Ni as well as patches of C and Al.

Al-Ca-Na were found in both the inclusions and the matrix (not shown here). In a few cases, Cr was found usually accompanied by Al, and this included an absence of Mg and Si (Figs. 3.33 and 3.34). Carbon was generally found in small areas scattered throughout the meteorite. Upon further investigation at higher resolutions, C was mainly in the form of smooth structures of about 10 to 20 microns in size (Figs. 3.29 and 3.35).

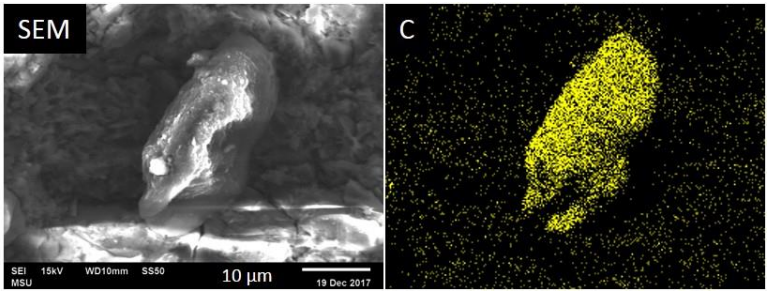

Figure 3.29: SEM image and EDS map of spot 6 of inclusion 2 (marked in Fig. 3.28) in Murray at 2300X magnification. SEM image shows a smooth, ~10 µm sized structure corresponding to C in the EDS map.

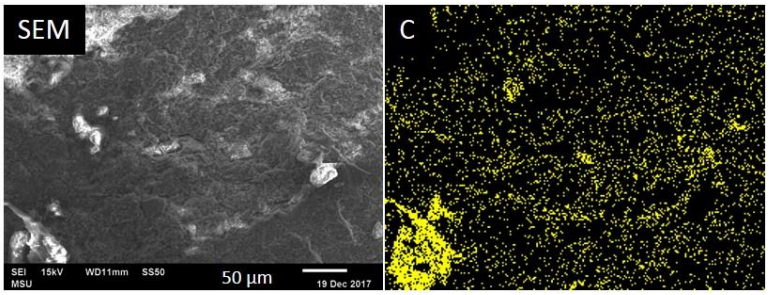

Figure 3.30: SEM image and EDS map of spot 9 of inclusion 2 (marked in Fig. 3.28) in Murray at 300X magnification. EDS map shows patches of C.

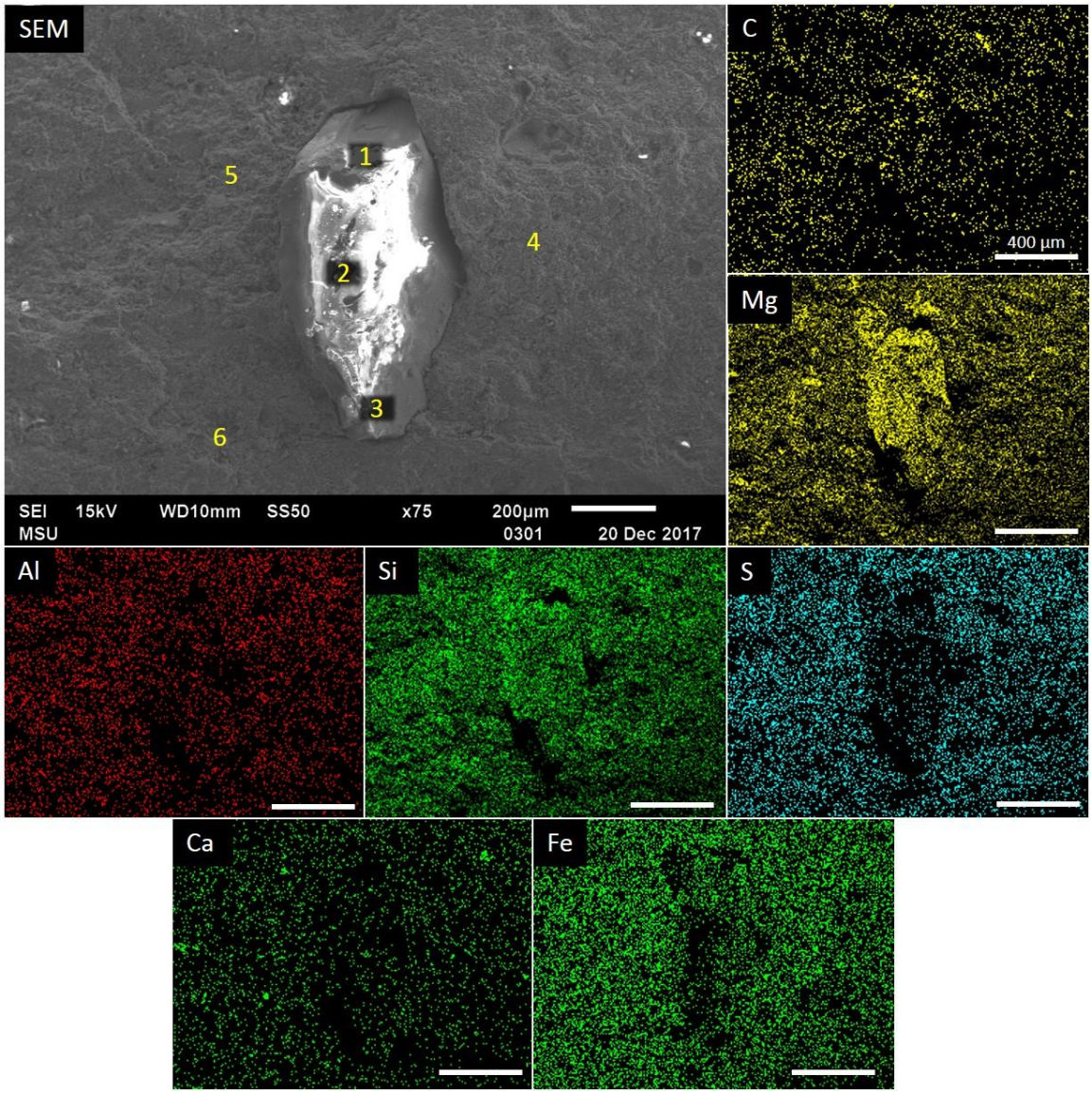

Figure 3.31: SEM image and EDS maps of inclusion 3 and surrounding matrix in Murray at 75X magnification. SEM image shows the topography of the well-defined inclusion and adjacent matrix. Yellow numbers in the SEM image indicate the locations of spots used for higher magnification data. EDS maps show a correlation between Mg-Si and Fe-S as well as patches of Al and Ca.

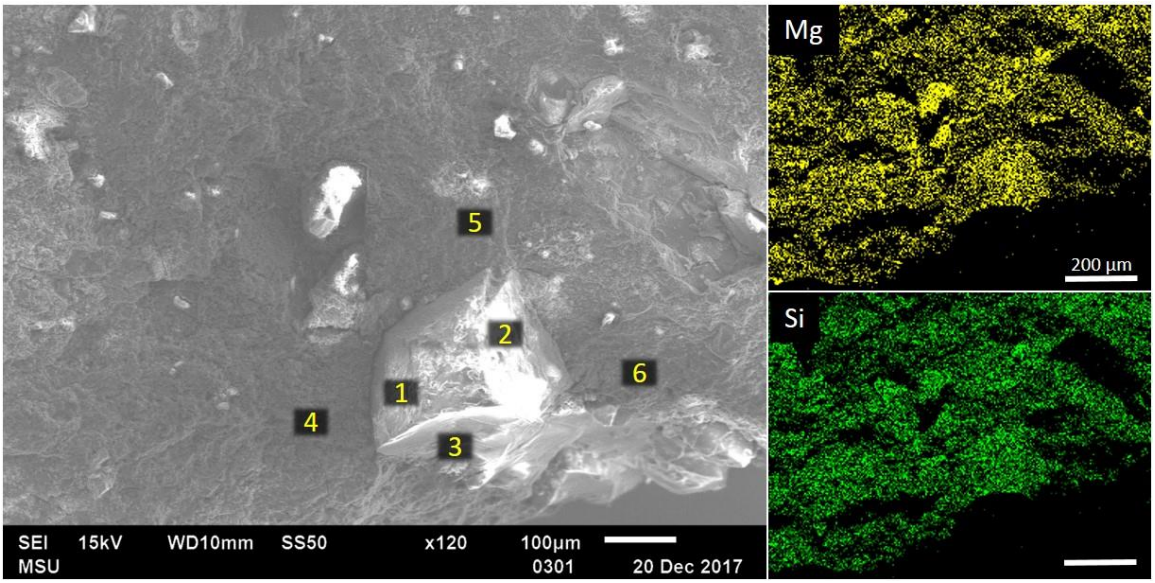

Figure 3.32: SEM image and EDS maps of inclusion 4 and surrounding matrix in Murray at 120X magnification. SEM image shows the topography of the well-defined inclusion and adjacent matrix. Yellow numbers in the SEM image indicate the locations of spots used for higher magnification data. EDS maps show a correlation between Mg-Si.

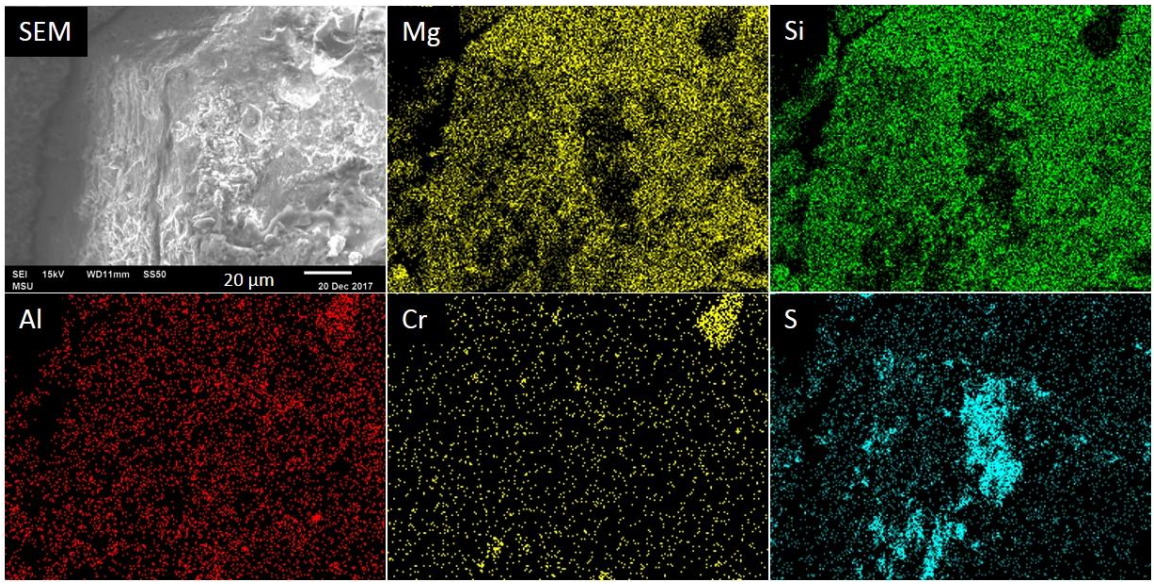

Figure 3.33: SEM image and EDS maps of spot 1 of inclusion 4 (marked in Fig. 3.32) in Murray at 800X magnification. EDS maps show correlations between Mg-Si and Al-Cr as well as patches of S.

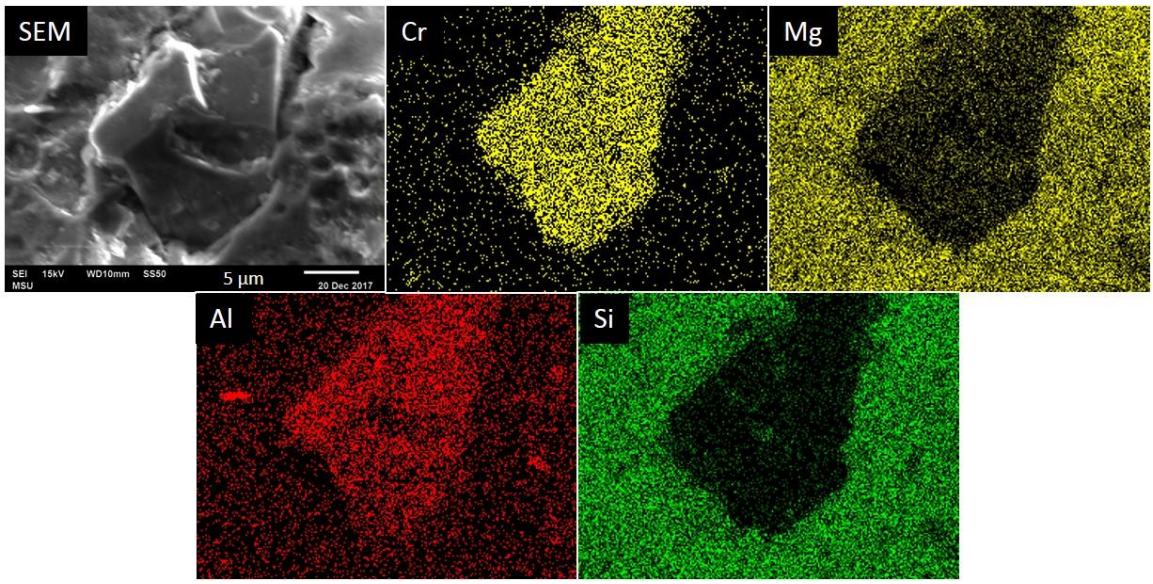

Figure 3.34: SEM image and EDS maps of spot 2 of inclusion 4 (marked in Fig. 3.32) in Murray at 3700X magnification. EDS maps show correlations between Mg-Si and Al-Cr.

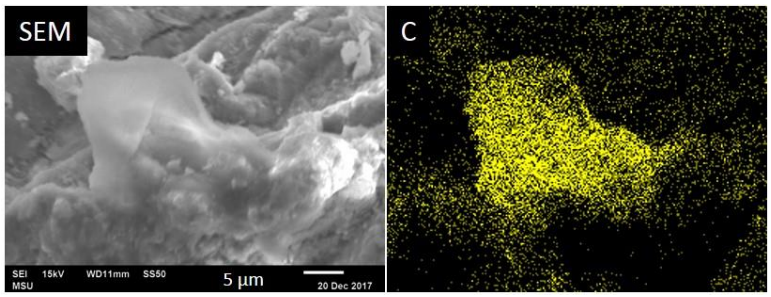

Figure 3.35: SEM image and EDS map of spot 6 of inclusion 4 (marked in Fig. 3.32) in Murray at 2700X magnification. SEM image shows a smooth, ~20 µm sized structure corresponding to C in the EDS map.

Table 3.2 gives the percentage by weight ranges retrieved from the data of whole inclusion views in Murray (Figs. 3.26, 3.28, 3.31, 3.32, 3.36, and 3.37) and the bulk mean composition for CM chondrites from Hutchison (2004). Even with the differing inclusion sizes and magnifications used for imaging, the relative abundance of elements kept the

same order. The major elements were O, Fe, Si, and Mg; the minor elements were C, S, Ni, and Ca; and the trace elements were Al, Na, and Cr.

Murray CM2 Meteorite											
Element (wt. %)	O	Fe	Si	Mg	C	S	Ni	Ca	Al	Na	Cr
This Study	34.0-38.0	23.5-30.5	11.5-13.0	9.0-13.0	4.5-6.5	3.0-4.5	1.5-2.5	1.0-1.5	0.5-1.0	0.5-1.0	0.5-1.0
Hutchison 2004	32.0	21.0	12.9	11.7	2.2	3.3	1.2	1.3	1.2	0.4	0.3

Table 3.2: Element wt. % range for whole inclusions and surrounding matrix in Murray obtained in this study and the bulk mean composition for CM chondrites reported in Hutchison 2004.

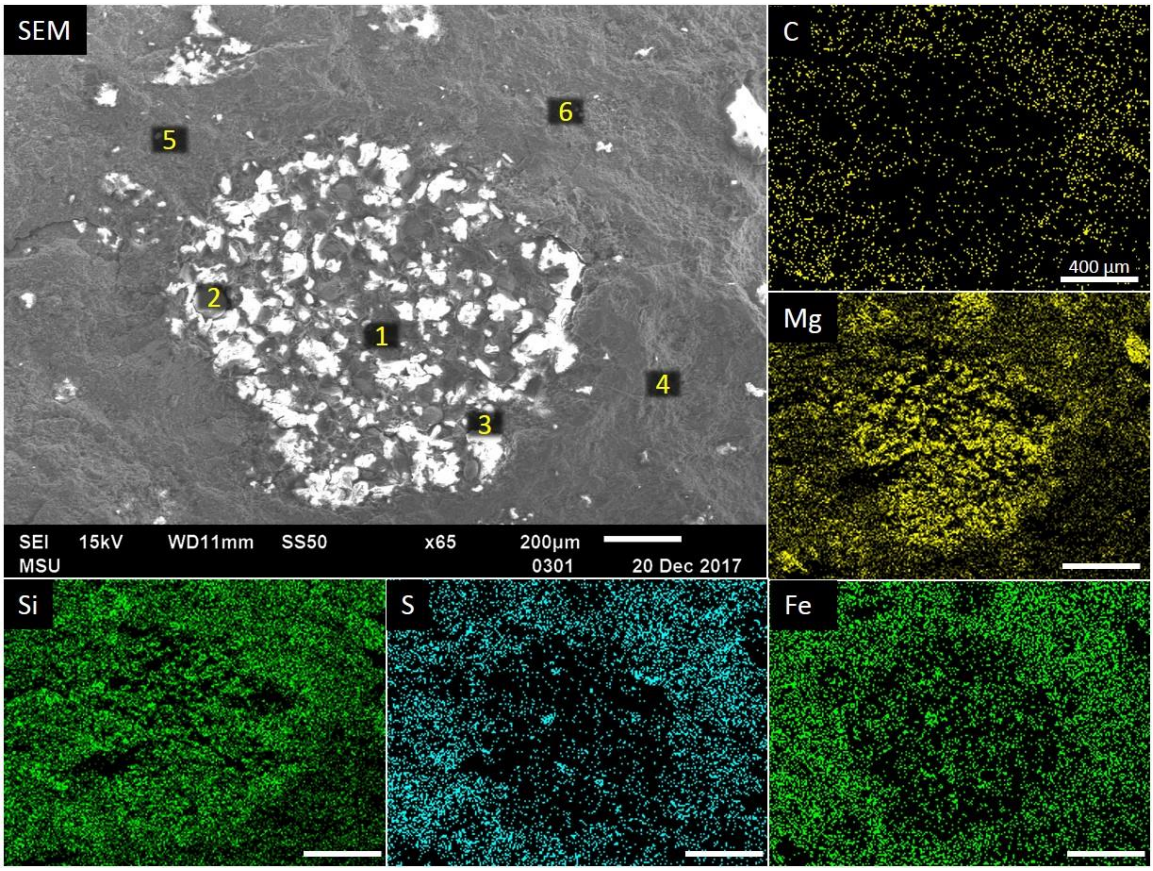

Figure 3.36: SEM image and EDS maps of inclusion 5 and surrounding matrix in Murray at 65X magnification. SEM image shows the topography of the well-defined inclusion and adjacent matrix. Yellow numbers in the SEM image indicate the locations of spots used for higher magnification data. EDS maps show correlations between Mg-Si and Fe-S as well as a higher relative concentration of C in the matrix.

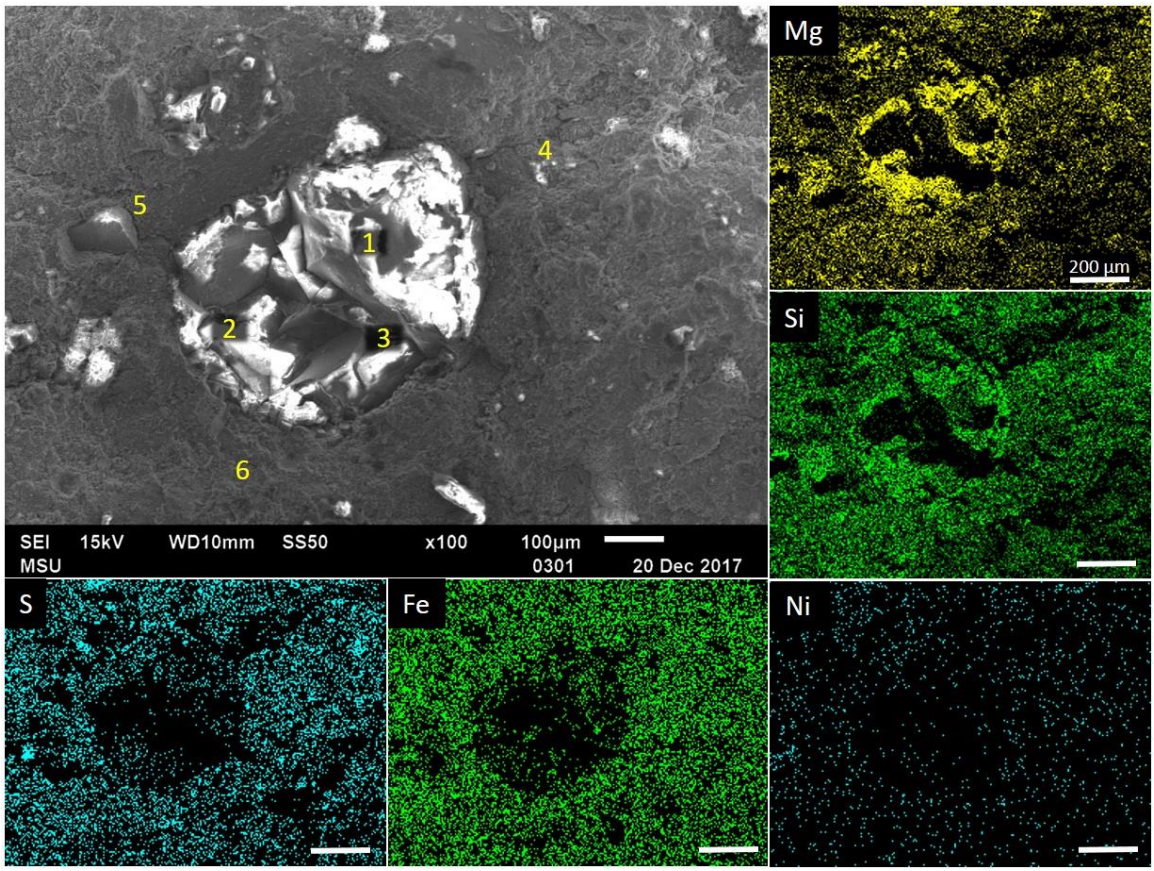

Figure 3.37: SEM image and EDS maps of inclusion 6 and surrounding matrix in Murray at 100X magnification. SEM image shows the topography of the well-defined inclusion and adjacent matrix. Yellow numbers in the SEM image indicate the locations of spots used for higher magnification data. EDS maps show correlations between Mg-Si and Fe-S-Ni.

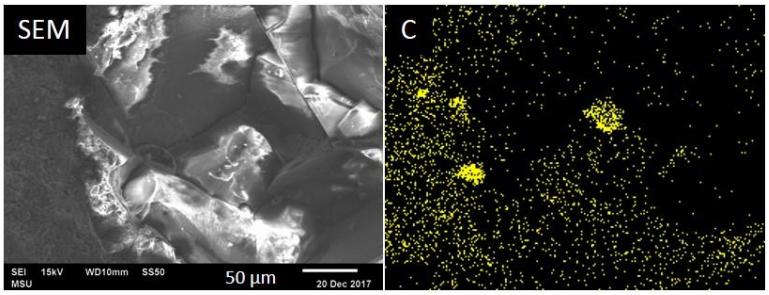

Figure 3.38: SEM image and EDS map of spot 2 of inclusion 6 (marked in Fig. 3.37) in Murray at 370X magnification. EDS map shows patches of C.

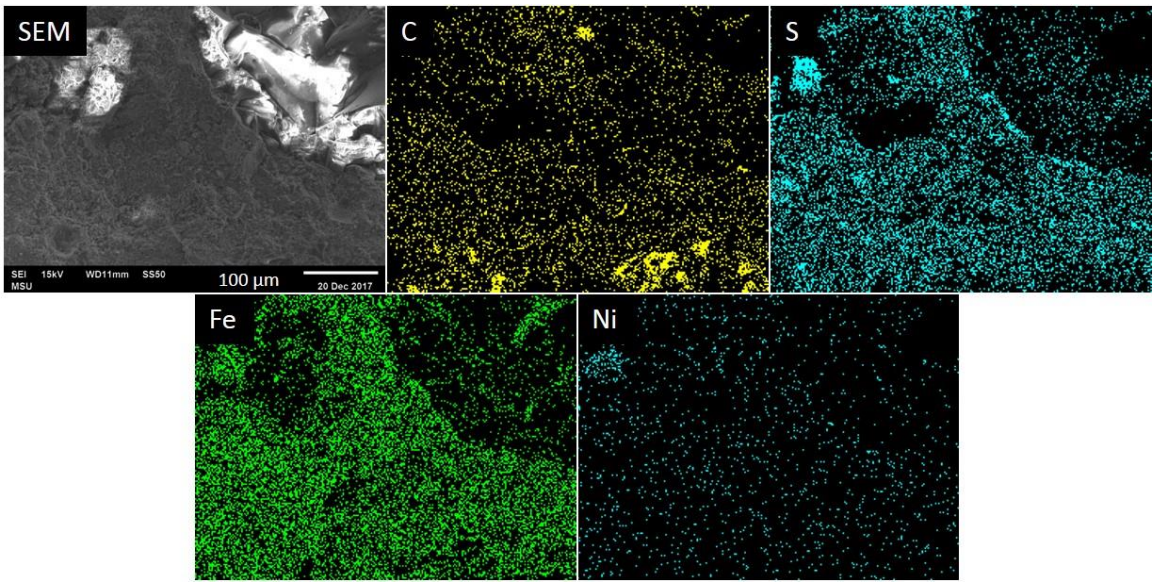

Figure 3.39: SEM image and EDS maps of spot 6 of inclusion 6 (marked in Fig. 3.37) in Murray at 250X magnification. EDS maps show a correlation between Fe-S-Ni as well as patches of C.

4. Discussion

4.1 Comparisons within Chondrites

In Moss, inclusions 6, 7, 11, and 12 (Figs. 2.3a, 3.2, 3.7, 3.11, and 3.17) looked similar to each other under both the optical microscope/Raman probe camera as well as under the SEM. Optically, these inclusions were a combination of dark grey and brown, with shiny specks scattered throughout. Inclusions 6, 7, and 11 also contained rims, veins, or fragments of Fe-S (Figs. 3.2-3.4, 3.7, 3.10, and 3.11). Inclusion 13 (Fig. 3.21) looked different under the two instruments when compared to inclusions 6, 7, 11, and 12. Optically, this inclusion was mostly white. All five inclusions displayed Raman spectra of forsterite and/or enstatite as well as higher relative concentrations of Mg-Si-O inside of their boundaries. The EDS, Raman, and optical data confirm that all five inclusions are chondrules. The elemental composition of Moss (Table 3.1) is in good agreement with the literature for CO chondrites; the range of values for most elements in this work envelop the mean bulk chemical composition or differ by less than ~10% (Hutchison 2004).

In Murray, inclusions 1, 3, 4, and 6 (Figs. 2.3b, 3.26, 3.31, 3.32, and 3.37) appeared similar to each other under both optical inspection and the electron microscope. These inclusions looked to be green crystals (Fig. 4.1), the Raman spectra showed very intense olivine peaks (specifically forsterite), and the EDS maps showed higher relative concentrations of Mg-Si-O inside the boundaries of the inclusions. These data lead to the conclusion that inclusions 1, 3, 4, and 6 are olivine crystals. Inclusions 2 and 5 (Figs. 3.28 and 3.36) were representative of many other inclusions (not studied here) throughout the sample, and seemed to be composed of many, smaller, white inclusions. The main

difference was that inclusion 2 contained a circular Fe-S center. These smaller white inclusions had higher relative Mg-Si-O concentrations than the surrounding matrix, and the Raman spectroscopy data indicated the presence of forsterite. This optical, mineralogical, and elemental data leads inclusions 2 and 5 to be classified as chondrules. Murray also contained the Raman spectra of at least three unknown minerals (Figs. 3.25d, 3.25e, and 3.25f). Other articles and the RRUFF database were investigated while considering the elements present from EDS, but no consensus can currently be made. Comparing with another work considering Raman spectra (Hanesch 2009), the minerals in Figure 3.25 e) and f) could be an iron-oxide, an iron-hydroxide, or some type of intermediate transformation of these. Overall, the elemental composition of Murray (Table 3.2) is also in good agreement with CM chondrites as seen in the literature and most values fall within the same thresholds as given for Moss (Hutchison 2004).

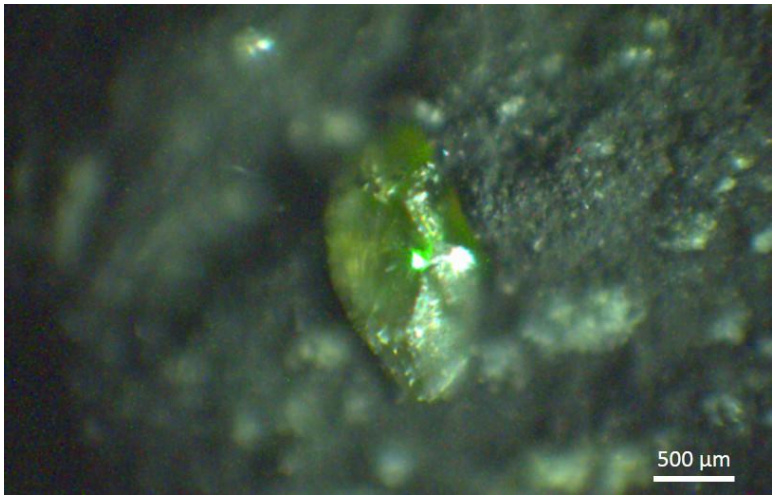

Figure 4.1: Representative micrograph of the olivine crystals found in Murray (inclusion 3). The green laser spot used for Raman spectroscopy data can be seen along with an internal reflection.

It is not clear yet how the aforementioned minerals were formed in the inclusions or matrix. For instance, several explanations about the formation of the forsterite crystals

are discussed in the literature. They may have been formed by disaggregation of chondrules, or by condensation from the solar nebula being a significant constituent of chondrule precursor material (Scott and Krot 2007 and references therein). The relatively large size of the crystals (Fig. 4.1) would imply slow cooling rates during initial formation (Hutchison 2004; Sears 2005).

4.2 Comparisons between Chondrites

Moss and Murray did display a number of similarities. The minerals of forsterite and enstatite were the dominant Raman signals for olivine and pyroxene, respectively. Graphitic carbon Raman signals were present in both samples as well. Both chondrites contained the same major elements (O, Fe, Mg, Si), mostly the same minor elements (C, S, Ni, Ca), and mostly the same trace elements (Na, Cr). Only Al varied between the two and this was only by ~1 wt. %. In each sample, when Fe-S or Fe-Ni were together there was a lack of Mg-Si-O, and vice versa. Also, the C spots in both appear to be smooth and did not display any particular structure from common carbon allotropes (e.g. carbon nanotubes, fullerenes, nanodiamonds). This is consistent with the Raman signals of graphitic carbon with defective or incomplete structures. Opportunity for further study could include investigating if other C structures with undetected Raman signals could be present in the studied or in other regions using higher resolution SEM imaging since they have been observed in other meteoritic samples (Abdu et al. 2018; Fries and Steele 2008). Finally, both samples contained patches that consisted of some combination of Al-Ca-Na throughout both the inclusions and matrix.

Inclusions followed the typical definition of chondrules (Section 1.2.3) in Moss while Murray contained both crystals and chondrules. The chondrules of Moss were composed of three different minerals (Section 3.1.1) and Murray's chondrules and crystals contained primarily forsterite (Section 3.2.1). Graphitic carbon was found almost exclusively in matrix throughout Murray (Section 3.2.1) while five different minerals were found in the matrix of Moss (Section 3.1.1). These minerals and their locations can be seen in Table 4.1. Graphitic carbon in Moss had well-defined D- and G-bands while Murray's bands presented a much lower signal-to-noise ratio along with a high fluorescence background. This carbon band variation can be the result of differing types and degrees of alteration in each of the samples – the more ordered the structure is, the more well-defined the bands will be (Bonal et al. 2016; Busemann et al. 2007; Homma et al. 2015). While both samples contained Fe-S, in Moss it appeared shiny and bronze colored under the optical microscope while in Murray it was dark grey and dull. This could be due to differing relative amounts of Fe and S or the presence of other elements, such as O, Cr, and/or Ni.

Sample	Location	Mineral					
		Graphitic Carbon	Forsterite	Enstatite	Hematite	Magnetite	Unidentified
Moss	Inclusions	✓	✓	✓			
	Matrix	✓	✓	✓	✓	✓	
Murray	Inclusions		✓	✓			✓
	Matrix	✓					✓

Table 4.1: Mineral comparisons of the inclusions and matrix in both the Moss and Murray samples.

4.3 Iron-Sulfur Relations

In both Moss and Murray there were pieces, veins, rims, and whole areas of Fe-S present. Troilite (FeS) was the first possibility since it is a common mineral found in meteorites (Hutchison 2004; McSween, Jr. and Huss 2010; Rubin and Varela 2018;

Sears 2005). To test this, the point-and-shoot feature on the SEM/EDS was utilized while considering the Fe:S stoichiometric ratios for troilite and other Fe-S minerals, such as pyrite (FeS_2) and pyrrhotite ($Fe_{0.8\text{-}1.0}S$): 1, 0.5, and ~0.875, respectively (Losh 2018). The data gave inconclusive results. The mean iron-to-sulfur ratio in Moss was ~1.70 (with the lowest individual value being 1.54) and in Murray the mean ratio was ~2.70 (with the lowest single value of 2.01). Patches of almost pure iron were found while performing the point-and-shoot measurements indicating the presence of elemental iron-metal or other minerals that contain Fe. In addition, Raman spectroscopy data from areas containing Fe-S were inconclusive due to very poor signals.

The formation of these rims, veins, and fragments is still not fully understood. Calculations predict that Fe-S should combine in nebular reactions to form troilite but this was probably not preserved in original form due to later thermal alteration (McSween, Jr. and Huss 2010). One explanation compares these rims to the fusion crust found on meteorites. The parent chondrite may have entered a large body's atmosphere and this allowed for combination of Fe-S, Fe-Ni, or just the accretion of Fe around the chondrule. A second possibility is that chondrules were originally free-floating in the solar nebula. The rim materials were originally nebular dust that stuck on to the chondrules. Another option is that the rims accreted to the chondrule while it was cooling, so both formations were contemporary (Sears 2005 and references therein).

4.4 Carbon Peak Parameters and Peak Metamorphic Temperature (PMT)

The peak metamorphic temperature (PMT) on the parent body of the meteorite can give information about the formation environment and ensuing alteration. One way to determine the PMT of a sample is to use Raman thermometry of the carbon bands in a sample. Multiple authors (Aoya et al. 2010; Beyssac et al. 2002; Busemann et al. 2007; Homma et al. 2015; Kouketsu et al. 2013; Rahl et al. 2005) have modelled PMTs as functions of the full width at half maximum (FWHM – symbolized here as Γ) of the D-bands. The Γ of the D-bands (Γ_D) correlate to petrologic type and metamorphism better than the Γ of the G-bands (Bonal et al. 2016; Busemann et al. 2007). Data can be taken from many points inside of the sample (from inclusions and the matrix) and averaged to give one Γ value for the entire meteorite. These models could be applied in this research to Moss but not to Murray due to the poor graphitic carbon signals in Murray. This is because Murray is a relatively unweathered, pristine CM2 sample (Busemann et al. 2007).

After applying the different models (see respective author's works cited here for parameter determination) the methods of Busemann et al. (2007) and Homma et al. (2015) gave values that best matched the current literature about PMTs experienced by the parent bodies (Section 1.2.2). Using the Busemann procedure, a Γ_D value of $(68 \pm 8)\ \mathrm{cm}^{-1}$ is obtained which is agreement with the other CO chondrites and meteorites of similar petrologic type. The Busemann model for PMT is given by the equation:

$$PMT(^{\circ}\mathrm{C}) = 931 - (5.10 * \Gamma_D * \mathrm{cm}) + [0.0091 * (\Gamma_D * \mathrm{cm})^2] \qquad (4.1)$$

and using the Γ_D from above gave a PMT value of (630 ± 20)°C, which is a bit higher than the uppermost accepted temperature for petrologic type 3 (Section 1.2.2). Using the

Homma procedure, a Γ_D value of (75 ± 3) cm^{-1} was obtained, which is in agreement with the other CO chondrites and meteorites of similar petrologic type. The Homma model for PMT is given by the equation:

$$PMT(°C) = -6.9 * \Gamma_D(cm^{-1}) + 1054.4 \quad (4.2)$$

and using the corresponding Γ_D gave a temperature of (540 ± 20)°C which is in good agreement with the accepted range for petrologic type 3.6 chondrites (Huss et al. 2006; Hutchison 2004; McSween, Jr. and Huss 2010; Norton and Chitwood 2008; Scott 2007).

These high, type 3 PMTs acquired correspond to more graphitization (better graphitic structure and therefore higher signal-to-noise ratios, Huck et al. 2003) and more thermal metamorphism in the parent body (Beyssac et al. 2002; Bonal et al. 2016; Busemann et al. 2007; Homma et al. 2015).

5. Conclusions

In this work, two carbonaceous chondritic fragments, Moss and Murray, were studied with the objective of determining their compositions in detail; thus to contribute more information about these meteorites and add to previous works.

Raman spectroscopy and SEM/EDS provided beneficial means to characterize the mineralogical, topographic, and elemental compositions of the meteoritic samples. Raman spectroscopy indicated in Moss the presence of graphitic carbon, forsterite (Mg-rich olivine), and enstatite (Mg-rich pyroxene) in the chondrules; Raman data from Murray included at least two unknown minerals in the chondrules while only forsterite was found in the crystal inclusions. The matrix of Moss contained graphitic carbon, forsterite, enstatite, hematite, and magnetite while in Murray's matrix, graphitic carbon, enstatite, and an unknown mineral or combination of minerals were present. The SEM micrographs displayed well-defined chondrules in Moss along with both olivine crystals and chondrules in Murray. The EDS maps presented correlations between Mg-Si-O inside of the inclusions (both for chondrules and crystals) and higher relative amounts of Fe in the surrounding matrix for both samples. Iron-sulfur combinations were found as rims and veins near the chondrules in Moss and as a chondrule-like fragment in Murray; however, it is inconclusive as to which Fe-S mineral(s) are contained in either sample.

These results demonstrate an agreement between the minerals obtained from Raman spectroscopy and the elements found using EDS. The data acquired from both of these techniques are consistent with the current literature for CO3.6 and CM2 chondrites.

The D-band fitting in Moss showed carbon structures with relatively high graphitization. This would imply the parent body of Moss experienced some type of secondary process, i.e. thermal metamorphism. The PMT models applied showed that the Moss sample experienced relatively high temperatures (~540° to 630°C) on its parent body when compared to other petrologic type 3 chondrites (~350° to 600°C). Due to the high fluorescence and low signal-to-noise ratio in Murray, the degree of graphitization is relatively low. This is in agreement with other petrologic type 2 meteorites, as they have experienced relatively little thermal metamorphism.

Even though several implications have been discussed in the literature about the formation of these structures (such as those ones mentioned for the formation of forsterite crystals and Fe-S rims in Sections 4.1 and 4.3, respectively), more studies will need to be performed to unravel the mysteries surrounding the formation of these relics.

Acknowledgments

First of all, I would like to express my sincerest gratitude to my research advisor, Dr. Analía "Yanil" Dall'Asén. Without her guidance, training, ideas, and insights this project would never have come to fruition. I can confidently say that with her help I have become a more proficient scientist than when I started this degree.

Secondly, I would like to recognize all of the individuals who assisted me throughout my research experience: Dr. Russell Palma who served as a committee member and gave us access to his meteorite collection; Dr. Chad Wittkop for his service on my thesis committee; Dr. Michael Bentley for giving us training and access to the SEM/EDS; Dr. Steven Losh for his helpful Fe-S suggestions; Mr. Michael Peters for his technical support and laboratory expertise; fellow graduate student Raka Paul for her preliminary literature study; undergraduate student Rohil Kayastha for organizing and documenting the best samples to use.

Also, I would like to thank those who contributed to my academic success: the Department of Physics and Astronomy for giving me the opportunity to pursue my master's degree; Dr. Youwen Xu for giving me an appreciation for the rigors of physics; office mate and fellow graduate student Dylan Meyer for the many hours of working through assignments together and his role as a sounding board.

Last but not least, I am forever appreciative of the people who supported me personally: my parents, Robert and Jacqueline, and siblings, Paul and Rachel, for their love and understanding; my wife Elizabeth for her patience and willingness to surrender our time together as I spent countless hours on homework, grading, and writing this thesis.

References

Abdu Y. A., Hawthorne F. C., and Varela M. E. 2018. Infrared Spectroscopy of Carbonaceous-chondrite Inclusions in the Kapoeta Meteorite: Discovery of Nanodiamonds with New Spectral Features and Astrophysical Implications. *The Astrophysical Journal Letters* 856:L9.

Aoya M., Kouketsu Y., Endo S., Shimizu H., Mizukami T., Nakamura D., and Wallis S. 2010. Extending the applicability of the Raman carbonaceous-material geothermometer using data from contact metamorphic rocks. *Journal of Metamorphic Geology* 28:895–914.

Bernatowicz T., Fraundorf G., Ming T., Anders E., Wopenka B., Zinner E., and Fraundorf P. 1987. Evidence for interstellar SiC in the Murray carbonaceous meteorite. *Nature* 330:728–730.

Beyssac O., Goffé B., Chopin C., and Rouzaud J. N. 2002. Raman spectra of carbonaceous material in metasediments: a new geothermometer. *Journal of Metamorphic Geology* 20:859–871.

Bonal L., Quirico E., Bourot-Denise M., and Montagnac G. 2006. Determination of the petrologic type of CV3 chondrites by Raman spectroscopy of included organic matter. *Geochimica et Cosmochimica Acta* 70:1849–1863.

Bonal L., Quirico E., Flandinet L., and Montagnac G. 2016. Thermal history of type 3 chondrites from the Antarctic meteorite collection determined by Raman spectroscopy of their polyaromatic carbonaceous matter. *Geochimica et Cosmochimica Acta* 189:312–337.

Bouvier A., Wadhwa M., Siman S. B., and Grossman L. 2013. Magnesium isotopic fractionation in chondrules from the Murchison and MurrayCM2 carbonaceous chondrites. *Meteoritics & Planetary Science* 48:339–353.

Busemann H., Alexander M. O., and Nittler L. R. 2007. Characterization of insoluble organic matter in primitive meteorites by microRaman spectroscopy. *Meteoritics & Planetary Science* 42:1387–1416.

Campbell-Brown M., and Brown P. 2016. Meteors, Comets, and Dust. In *RASC 2017 Observer's Handbook*. Toronto: Royal Astronomical Society of Canada.

Chizmadia L. J., Rubin A. E., and Wasson J. T. 2002. Mineralogy and petrology of amoeboid olivine inclusions in CO3 chondrites: Relationship to parent-body aqueous alteration. *Meteoritics & Planetary Science* 37:1781–1796.

Connolly H. C. et al. 2007. The Meteoritical Bulletin, No. 91, 2007 March. *Meteoritics & Planetary Science* 42:413–466.

Dall'Asén A. G., Dimas S. I., Tyler S., Johnston J. F., Anderton T. R., Ivans I. I., Gerton J. M., Bromley B. C., and Kenyon S. J. 2017a. Mapping the composition of chondritic meteorite Northwest Africa 3118 with micro-Raman spectroscopy. *Spectroscopy Letters* 50:417–425.

Dall'Asén A. G., Mittelstaedt J., Kim J. S., Baer B., Paul R., Gerton J. M., Bromley B. C., and Kenyon S. J. 2017b. Comparative study of carbonaceous meteoritic fragments by micro-Raman spectroscopy and SEM/EDS. *APS April Meeting*, Washington D.C.

Dall'Asén A. G., Stokke A. R., Paul R., Kayastha R., Bromley B. C., and Kenyon S. J. 2018. Mineralogical and Elemental Composition of Carbonaceous Chondrites by micro-Raman Spectroscopy and SEM/EDS. *49th Lunar and Planetary Science Conference*, The Woodlands, Texas.

Dodd R. T. 1981. *Meteorites: A petrologic-chemical synthesis*, Cambridge Cambridgeshire; New York: Cambridge University Press.

Echlin P., Fiori C. E., Goldstein J., Joy D. C., and Newbury D. E. 1986. *Advanced Scanning Electron Microscopy and X-Ray Microanalysis*, Springer US.

Ferraro J. R., Nakamoto K., and Brown C. W. 2002. *Introductory Raman Spectroscopy*, San Diego, United States: Elsevier Science & Technology.

Fries M., and Steele A. 2008. Graphite Whiskers in CV3 Meteorites. *Science* 320:91–93.

Goldstein J. I., Newbury D. E., Michael J. R., Ritchie N. W. M., Scott J. H. J., and Joy D. C. 2018. *Scanning Electron Microscopy and X-Ray Microanalysis*, 4th ed. New York: Springer-Verlag.

Hafner B. 2015a. Scanning Electron Miscroscopy Primer.

Hafner B. 2015b. Energy Dispersive Spectroscopy on the SEM: A Primer.

Hanesch M. 2009. Raman spectroscopy of iron oxides and (oxy)hydroxides at low laser power and possible applications in environmental magnetic studies. *Geophysical Journal International* 177:941–948.

Homma Y., Kouketsu Y., Kagi H., Mikouchi T., and Yabuta H. 2015. Raman spectroscopic thermometry of carbonaceous material in chondrites: four–band fitting analysis and expansion of lower temperature limit. *Journal of Mineralogical and Petrological Sciences* 110:276–282.

Horan J. R. 1953. The Murray, Calloway County, Kentucky, Aerolite (cn =+0881,366)*. *Meteoritics* 1:114–121.

Huck H., Halac E. B., Reinoso M., Dall'Asén A. G., Somoza A., Deng W., Brusa R. S., Karwasz G. P., and Zecca A. 2003. Microstructural analysis of carbon films obtained from C_{60} fullerene ion beams. *Applied Surface Science* 211:379–385.

Huss G. R., Rubin A. E., and Grossman J. N. 2006. Thermal Metamorphism in Chondrites. In *Meteorites and the Early Solar System II*. Tuscon: The University of Arizona Press. pp. 567–586.

Hutchison R. 2004. *Meteorites: A Petrologic, Chemical and Isotopic Synthesis*, New York: Cambridge University Press.

Kouketsu Y., Mizukami T., Mori H., Endo S., Aoya M., Hara H., Nakamura D., and Wallis S. 2013. A new approach to develop the Raman carbonaceous material geothermometer for low-grade metamorphism using peak width. *Island Arc* 23:33–50.

Larkin P. 2011. *Infrared and Raman Spectroscopy; Principles and Spectral Interpretation: Principles and Spectral Interpretation*, Saint Louis: Elsevier.

Losh S. L. 2018. Private communication.

McSween, Jr. H. Y. 1979. Are carbonaceous chondrites primitive or processed? A review. *Reviews of Geophysics* 17:1059–1078.

McSween, Jr. H. Y., Lauretta D. S., and Leshin L. A. 2006. Recent Advances in Meteoritics and Cosmochemistry. In *Meteorites and the Early Solar System II*. Tuscon: The University of Arizona Press. pp. 53–66.

McSween, Jr. H. Y., and Huss G. R. 2010. *Cosmochemistry*, 1 edition. Cambridge; New York: Cambridge University Press.

Metzler K. 2004. Formation of accretionary dust mantles in the solar nebula: Evidence from preirradiated olivines in CM chondrites. *Meteoritics & Planetary Science* 39:1307–1319.

NASA.org. Solar System Exploration: In Depth. *Solar System Exploration: NASA Science*. https://solarsystem.nasa.gov/small-bodies/meteors-and-meteorites/in-depth

Norton O. R., and Chitwood L. 2008. *Field Guide to Meteors and Meteorites*, London: Springer-Verlag.

Palmer E. E., and Lauretta D. S. 2011. Aqueous alteration of kamacite in CM chondrites. *Meteoritics & Planetary Science* 46:1587–1607.

Quirico E., Borg J., Raynal P.-I., Montagnac G., and d'Hendecourt L. 2005. A micro-Raman survey of 10 IDPs and 6 carbonaceous chondrites. *Planetary and Space Science* 53:1443–1448.

Quirico E., Montagnac G., Rouzaud J.-N., Bonal L., Bourot-Denise M., Duber S., and Reynard B. 2009. Precursor and metamorphic condition effects on Raman spectra of poorly ordered carbonaceous matter in chondrites and coals. *Earth and Planetary Science Letters* 287:185–193.

Rahl J. M., Anderson K. M., Brandon M. T., and Fassoulas C. 2005. Raman spectroscopic carbonaceous material thermometry of low-grade metamorphic rocks: Calibration and application to tectonic exhumation in Crete, Greece. *Earth and Planetary Science Letters* 240:339–354.

Raman C. V. 1929. Part II.—The Raman effect. Investigation of molecular structure by light scattering. *Transactions of the Faraday Society* 25:781–792.

Rubin A. E. 2010. Physical properties of chondrules in different chondrite groups: Implications for multiple melting events in dusty environments. *Geochimica et Cosmochimica Acta* 74:4807–4828.

Rubin A. E., and Grossman J. N. 2010. Meteorite and meteoroid: New comprehensive definitions. *Meteoritics & Planetary Science* 45:114–122.

Rubin A. E., and Varela M. E. 2018. Private communication.

RRUFF.info. Database of Raman spectroscopy, X-ray diffraction and chemistry of minerals. http://rruff.info/

Scott E. R. D. 2007. Chondrites and the Protoplanetary Disk. *Annual Review of Earth and Planetary Sciences* 35:577–620.

Scott E. R. D., and Krot A. N. 2007. 1.07 - Chondrites and Their Components. In *Treatise on Geochemistry*, edited by Holland H. D., and Turekian K. K. Oxford: Pergamon. pp. 1–72.

Sears D. W. G. 2005. *The Origin of Chondrules and Chondrites*, 1 edition. Cambridge, UK ; New York: Cambridge University Press.

Serway R. A., and Jewett J. W. 2009. *Physics for Scientists and Engineers with Modern Physics*, 8 edition. Belmont, CA: Brooks Cole.

Shimizu K., and Mitani T. 2010. *New Horizons of Applied Scanning Electron Microscopy*, Berlin Heidelberg: Springer-Verlag.

Twelker E. 2018. Private communication.

Weisberg M. K., McCoy T. J., and Krot A. N. 2006. Systematics and Evaluation of Meteorite Classification. In *Meteorites and the Early Solar System II*. Tucson: The University of Arizona Press. p. 34.

Wood J. A. 2005. The Chondrite Types and Their Origins. In *Chondrites and the Protoplanetary Disk.* San Francisco: Astronomical Society of the Pacific. p. 953.

Yesiltas M., Glotch T. D., and Ebel D. S. 2016. Molecular Constituents of the Moss (CO3.6) Chondrite via Micro-Raman Spectroscopic Imaging. *47th Lunar and Planetary Science Conference*, The Woodlands, Texas.

Zolensky M. E., Mittlefehldt D. W., Lipschutz M. E., Wang M.-S., Clayton R. N., Mayeda T. K., Grady M. M., Pillinger C., and B D. 1997. CM chondrites exhibit the complete petrologic range from type 2 to 1. *Geochimica et Cosmochimica Acta* 61:5099–5115.